Global and Planetary Change 197 (2021) 103387

Contents lists available at ScienceDirect

Global and Planetary Change

journal homepage: www.elsevier.com/locate/gloplacha

Marine osmium isotope record during the Carnian "pluvial episode" (Late Triassic) in the pelagic Panthalassa Ocean

Yuki Tomimatsu[a,b,*], Tatsuo Nozaki[c,d,e,f], Honami Sato[f,i], Yutaro Takaya[g,c,d,f], Jun-Ichi Kimura[h], Qing Chang[h], Hiroshi Naraoka[b], Manuel Rigo[i,j], Tetsuji Onoue[b]

[a] Department of Earth and Environmental Sciences, Kumamoto University, Kumamoto 860-8555, Japan
[b] Department of Earth and Planetary Sciences, Kyushu University, Fukuoka 812-8581, Japan
[c] Submarine Resources Research Center, Research Institute for Marine Resources Utilization, Japan Agency for Marine-Earth Science and Technology (JAMSTEC), Kanagawa 237-0061, Japan
[d] Frontier Research Center for Energy and Resources, The University of Tokyo, Tokyo 113-8656, Japan
[e] Department of Planetology, Kobe University, Hyogo 657-8501, Japan
[f] Ocean Resources Research Center for Next Generation, Chiba Institute of Technology, Chiba 275-0016, Japan
[g] Faculty of Science and Engineering, Waseda University, Tokyo 169-8555, Japan
[h] Volcanoes and Earth's Interior Research Center, Research Institute for Marine Geodynamics, Japan Agency for Marine-Earth Science and Technology (JAMSTEC), Kanagawa 237-0061, Japan
[i] Department of Geosciences, University of Padova, Padova 35131, Italy
[j] Institute of Geosciences and Earth Resource (IGG–CNR), Padova 35131, Italy

ARTICLE INFO

Keywords:
Osmium isotopes
Chert
Carnian Pluvial Episode
Wrangellia Flood Basalt
Mino Belt
Japan

ABSTRACT

The Carnian Pluvial Episode (CPE) was a global environmental change and biotic crisis that occurred during the Carnian (Late Triassic). The climate during the CPE was characterized by a short-lived period of extreme rainfall, and an extinction of marine taxa is known to have occurred during the latest Julian (i.e. early Carnian). Although these events are considered to have been caused by the Wrangellia Flood Basalt (FB) volcanism, existing studies have found little direct evidence to support this. We investigated the temporal relationship between the eruption of Wrangellia FB and CPE using high-resolution microfossil biostratigraphy and paleo-seawater Os isotope data of an Upper Triassic bedded chert succession from an accretionary complex in Japan, which accumulated in a pelagic deep-sea environment in an equatorial region of the Panthalassa Ocean. Our biostratigraphic analysis, based on conodonts and radiolarians, and osmium isotope data show: (i) a continuous decline of initial Os isotope ratios ($^{187}Os/^{188}Os_i$) in the early Julian; (ii) low $^{187}Os/^{188}Os_i$ ratios during the late Julian; and (iii) an abrupt increase in $^{187}Os/^{188}Os_i$ ratios at the end of the Julian. The decrease in $^{187}Os/^{188}Os_i$ ratios throughout the Julian suggests an increased input of unradiogenic Os from the eruption of the Wrangellia FB into the ocean. Moreover, redox-sensitive elements, such as V and U, increased abruptly at the end of the Julian, which is the first evidence of reducing conditions during the CPE within the pelagic deep-sea Panthalassa Ocean. Marine anoxic event in the late Julian has been recognized from widespread deposition of black shales and organic-rich marls in intermediate to shallow water Tethyan sections. Thus, oxygen-depleted conditions occurred at the Tethyan shallow continental margin, as well as in the pelagic deep-sea Panthalassa Ocean, at the end of Wrangellia FB volcanism.

1. Introduction

The Late Triassic was a prolonged (~36 Myr) interval characterized by major biotic turnover events prior to the end-Triassic extinction (e.g. Tanner et al., 2004; Ogg, 2012; Lucas and Tanner, 2018). One of the most dramatic events occurred during the Carnian (237.0–221.0 Ma for the "Long Tuvalian" option; 237.0–228.4 Ma for the "Long Rhaetian" option; Ogg, 2012). The Carnian is subdivided into the Julian and Tuvalian substages; the Julian–Tuvalian boundary occurs at ca. 232.0 or 233.5 Ma, respectively corresponding to the "Long Tuvalian" or "Long Rhaetian" options (Ogg, 2012). The dramatic events during the Carnian included major extinctions of marine taxa, such as crinoids, echinoids, bivalves, bryozoans, ammonoids, and conodonts in the Tethyan realm (Simms and Ruffell, 1989, 1990, 2018; Simms et al., 1995; Rigo et al.,

---

* Corresponding author at: Department of Earth and Environmental Sciences, Kumamoto University, Kumamoto 860-8555, Japan.
E-mail address: 172d9008@st.kumamoto-u.ac.jp (Y. Tomimatsu).

https://doi.org/10.1016/j.gloplacha.2020.103387
Received 9 April 2020; Received in revised form 11 October 2020; Accepted 22 November 2020

2007, 2018), and these extinctions of marine taxa are known to have occurred during the latest Julian (e.g. Dal Corso et al., 2018). On land, major turnovers in tetrapod vertebrates have been documented in the late Carnian (Benton, 1986; Furin et al., 2006; Lucas, 2018). However, some major groups originated and flourished in the late Carnian (Trotter et al., 2015), including dinosaurs on land (Benton et al., 2018; Bernardi et al., 2018), scleractinian reef builders (Stanley, 2003), and calcareous nannoplankton in an open-ocean environment (Erba, 2006; Preto et al., 2013). These biotic extinctions and turnover were associated with an not fully understood climate change event characterized by a short-lived period of extreme rainfall, termed the Carnian Pluvial Episode (CPE) (Simms and Ruffell, 1989).

The CPE occurred during the late Julian to early Tuvalian according to the biostratigraphy, and is known to have caused large-scale changes in many depositional environments from continental to deep-water settings (e.g. Simms and Ruffell, 1989; Simms et al., 1995; Rigo et al., 2007; Roghi et al., 2010; Ruffell et al., 2016). This event initially involved a major increase in siliciclastic influx and interrupted growth of carbonate platforms in Tethyan sections, along with the establishment of oxygen-depleted conditions in marginal basins and an increase in seawater temperatures (e.g. Hornung et al., 2007a, 2007b; Rigo et al., 2007; Nakada et al., 2014; Trotter et al., 2015; Mueller et al., 2016; López-Gómez et al., 2017; Baranyi et al., 2019; Jin et al., 2020). Although the cause of the CPE remains debated, a large volcanic event, such as the eruption of the Wrangellia Flood Basalt (FB), has been suggested as the most plausible trigger (Furin et al., 2006; Dal Corso et al., 2012). Previous U—Pb geochronological studies have yielded Wrangellia FB ages of 227.3 ± 2.6, 226.8 ± 0.5, 228.4 ± 2.5, and 232.2 ± 1.0 Ma (Mortensen and Hulbert, 1992; Parrish and McNicoll, 1992; Greene et al., 2010), and $^{40}Ar/^{39}Ar$ ages of the Wrangellia FB range from 233 to 227 Ma (Greene et al., 2010). The age of the Wrangellia FB is also constrained to the middle Ladinian and late Carnian by bivalve and ammonoid biostratigraphic data (e.g. Jones et al., 1977; Tozer, 1994). However, it is still unclear whether the peak eruptive phase of the Wrangellia FB coincided with the onset of the CPE, because only one radiometric age is available to provide internal constraints for the Carnian part of the timescale (Furin et al., 2006). Even if a detailed absolute timescale does not yet exist for the Carnian (Mundil et al., 2010; Ogg et al., 2014; Lucas, 2018), the Geomagnetic Polarity Time Scale for the entire Triassic (Maron et al., 2019) based on the recently verified Newark-Hartford astrochronological polarity time-scale (APTS) for the Late Triassic (Kent et al., 2017) constrained the Carnian stage.

In numerous studies, marine Os isotopic records preserved in pelagic sediments have been used to detect large volcanic inputs into the ocean; for example, the Deccan Traps at the end-Cretaceous (Ravizza and Peucker-Ehrenbrink, 2003; Robinson et al., 2009), the Caribbean–Colombian Plateau and Ontong Java Plateau eruptions in the mid-Cretaceous (Turgeon and Creaser, 2008; Tejada et al., 2009), and the Central Atlantic Magmatic Province at the end-Triassic (Kuroda et al., 2010). Marine Os isotope ratios reflect the relative balance between Os inputs from riverine water ($^{187}Os/^{188}Os \sim 1.4$) and hydrothermal fluids and extraterrestrial material ($^{187}Os/^{188}Os \sim 0.12$–$0.13$) into the ocean (Peucker-Ehrenbrink and Ravizza, 2000). Based on the release of unradiogenic Os from volcanic eruptions, unradiogenic Os isotope ratios in marine sediments may provide evidence of flood basalt eruptions (Cohen and Coe, 2002; Ravizza and Peucker-Ehrenbrink, 2003; Turgeon and Creaser, 2008; Tejada et al., 2009; Kuroda et al., 2010). The short residence time of Os in seawater allows whole-ocean shifts in isotopic composition to occur on short timescales (several tens of thousands of years; Levasseur et al., 1999), meaning the marine Os isotope record is a robust chemostratigraphic marker of flood basalt volcanism in the geological record.

Xu et al. (2014) reported a negative Os isotope excursion in the upper Ladinian shales from a boreal marine succession in Svalbard. This was used to infer that the Wrangellia volcanic activity initiated in the latest Ladinian. Recently, Nozaki et al. (2019) investigated the marine Os isotope record in a Triassic bedded chert succession from the Inuyama area, central Japan. They reported a continuous decrease in initial Os isotope ratios from the latest Ladinian to early Carnian, and attributed this to the eruption of the Wrangellia FB. In recent studies, the accurate calibration of chronostratigraphic stages and substages in the Carnian was established using ammonoids and conodonts (e.g. Mietto et al., 2012; Dal Corso et al., 2015, 2018; Sun et al., 2016; Jiang et al., 2019). In particular, a high-resolution conodont biostratigraphy described within the last ten years (Orchard, 2007, 2010; Rigo et al., 2007, 2018; Mazza et al., 2011, 2012) permits to improve the conodont biostratigraphy in the Carnian bedded chert successions in Japan (Yamashita et al., 2018).

In order to clarify the temporal relationship between the eruption of Wrangellia FB and CPE, we undertook a high-resolution, Os isotope and conodont–radiolarian biostratigraphic study of Carnian pelagic deep-sea sediments (bedded cherts) from the Panthalassa Ocean. Redox-sensitive elements (e.g. V, U, and Mo) and a carbon isotope profile of the bedded cherts were also used to elucidate the environmental changes during the CPE.

2. Geological setting and studied section

The studied section comprises Sections N and O of Sugiyama (1997), which are located in the Inuyama area, Mino Belt, central Japan (Fig. 1). The Mino Belt comprises a Jurassic subduction-generated accretionary complex and strikes in an approximately ENE–WSW direction in central Japan. The Mino Belt has been subdivided into six tectonostratigraphic units (Sakamoto-toge, Samondake, Funabuseyama, Nabi, Kanayama, and Kamiaso) on the basis of lithology, age, and structure (Wakita, 1988). The studied sections are in the Kamiaso unit (Wakita, 1988), which consists of thrust sheets of sedimentary sequences containing Triassic to Lower Jurassic bedded cherts and overlying Middle Jurassic clastic rocks (sandstone and mudstone; Fig. 1B; Matsuoka et al., 1994). The absence of carbonate rocks and coarse-grained terrigenous material in the Triassic–Jurassic bedded cherts suggests that the primary depositional site was deeper than the carbonate compensation depth, and beyond the reach of terrigenous clastic material (Matsuda and Isozaki, 1991). Paleomagnetic and biostratigraphic studies of the bedded cherts have shown that the site of deposition moved from low latitudes during the Middle Triassic to mid-latitudes during the Early Jurassic (Ando et al., 2001; Uno et al., 2015).

The chert–clastic sequence in the Inuyama area is exposed as a stack of thrust sheets (Wakita, 1988; Kimura and Hori, 1993). Yao et al. (1980) identified four chert thrust sheets, named CH-1, CH-2, CH-3, and CH-4, in structurally ascending order. The studied section (Sections N and O) are located in the CH-2 thrust sheet (Fig. 1C). Radiolarian and conodont biostratigraphic (e.g. Yao et al., 1980; Sugiyama, 1997; Onoue et al., 2012; Yamashita et al., 2018), magnetostratigraphic (Uno et al., 2015), and cyclostratigraphic (Ikeda et al., 2010; Ikeda and Tada, 2014; Ikeda et al., 2017) works have been conducted in the CH-2 chert successions.

Sections N and O in the Inuyama area (Fig. 2A) consist mainly of a succession of bedded cherts with a thickness of 13 and 8 m, respectively. In these sections, two lithological types of bedded cherts are observed: B- and F-type bedded cherts (Fig. 2B; Sugiyama, 1997). The B-type bedded cherts are characterized by a clear repetition of distinct siliceous and muddy layers with thicknesses of several centimeters. The F-type bedded cherts have indistinct boundaries due to amalgamation. Sections N and O consist mainly of B-type red cherts and F-type greenish gray cherts, with several intercalations of white chert layers (Sugiyama, 1997). These two sections can be correlated using a distinct white chert layer in the upper part of Section O and lower part of Section N (Nozaki et al., 2019). In this paper, we term the composite stratigraphic section of Sections N and O as the “Section N–O" (Fig. 3). A characteristic thick siliceous claystone bed, CS-1 (Sugiyama, 1997), is present in Section N—O at 9.4 m above the section base (Fig. 2C).

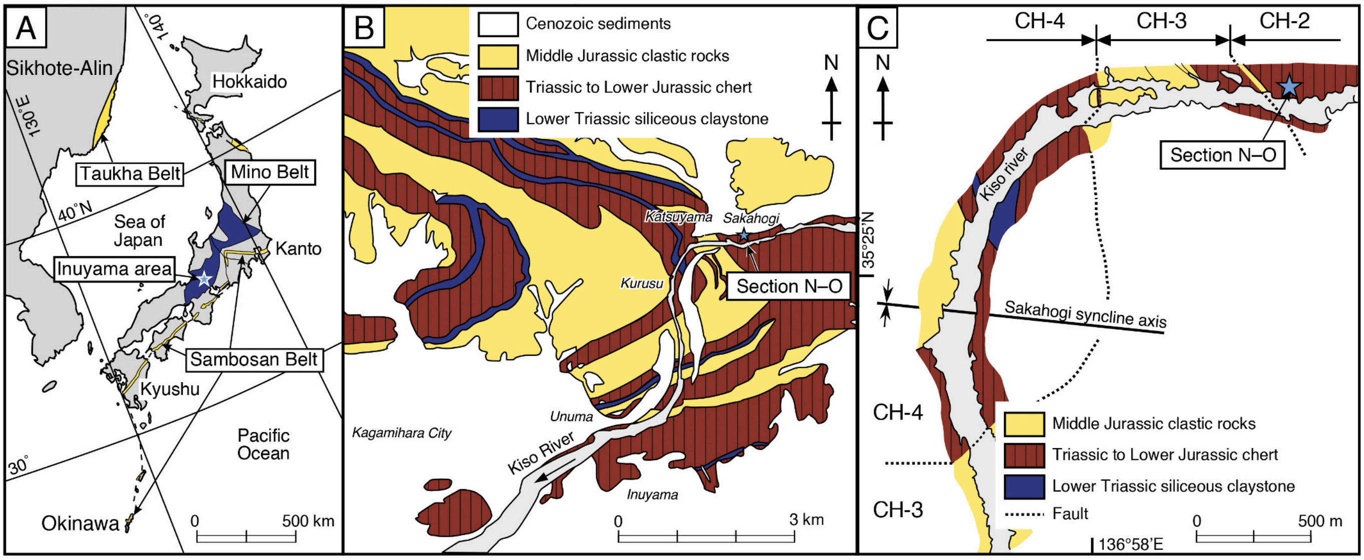

Fig. 1. A. Map showing the distribution of the Mino and Sambosan belts in Japan, and Taukha Belt in Far East Russia. B, C. Geological and route maps of the Inuyama area showing the locality of the study section along the middle reaches of Kiso River.

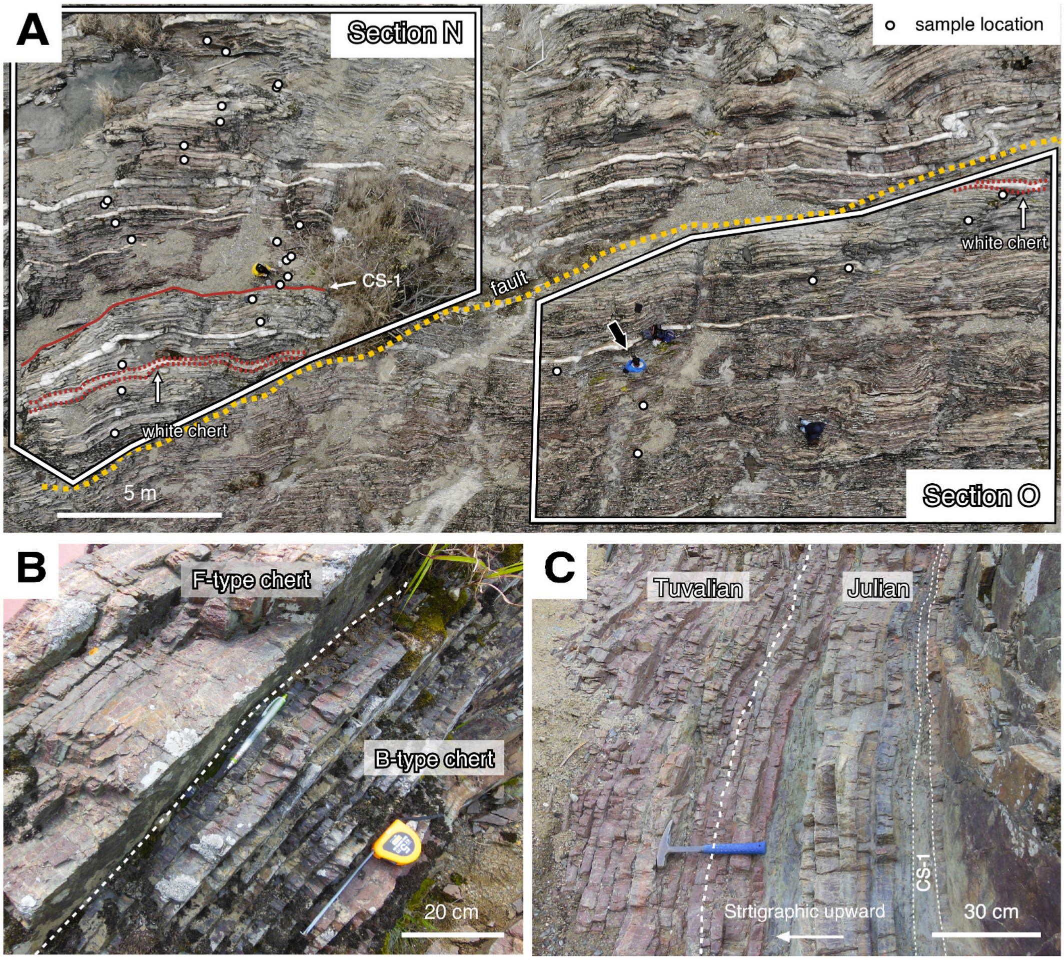

Fig. 2. A. Aerial outcrop photograph of Sections N—O (Sugiyama, 1997). Key beds of white chert in Section N—O are denoted with red dashed lines. Sample for Os isotope analysis. People for scale (denoted by arrows). B. Photograph of two types of bedded chert: B- and F-type bedded chert in Section N. C. Outcrop of the Julian–Tuvalian boundary in the bedded chert succession of Section N. The upper part of the Julian 2 bedded chert is greenish gray chert. The stratigraphic level of the CS-1 siliceous claystone (Sugiyama, 1997) is also shown. (For interpretation of the references to colour in this figure legend, the reader is referred to the web version of this article.)

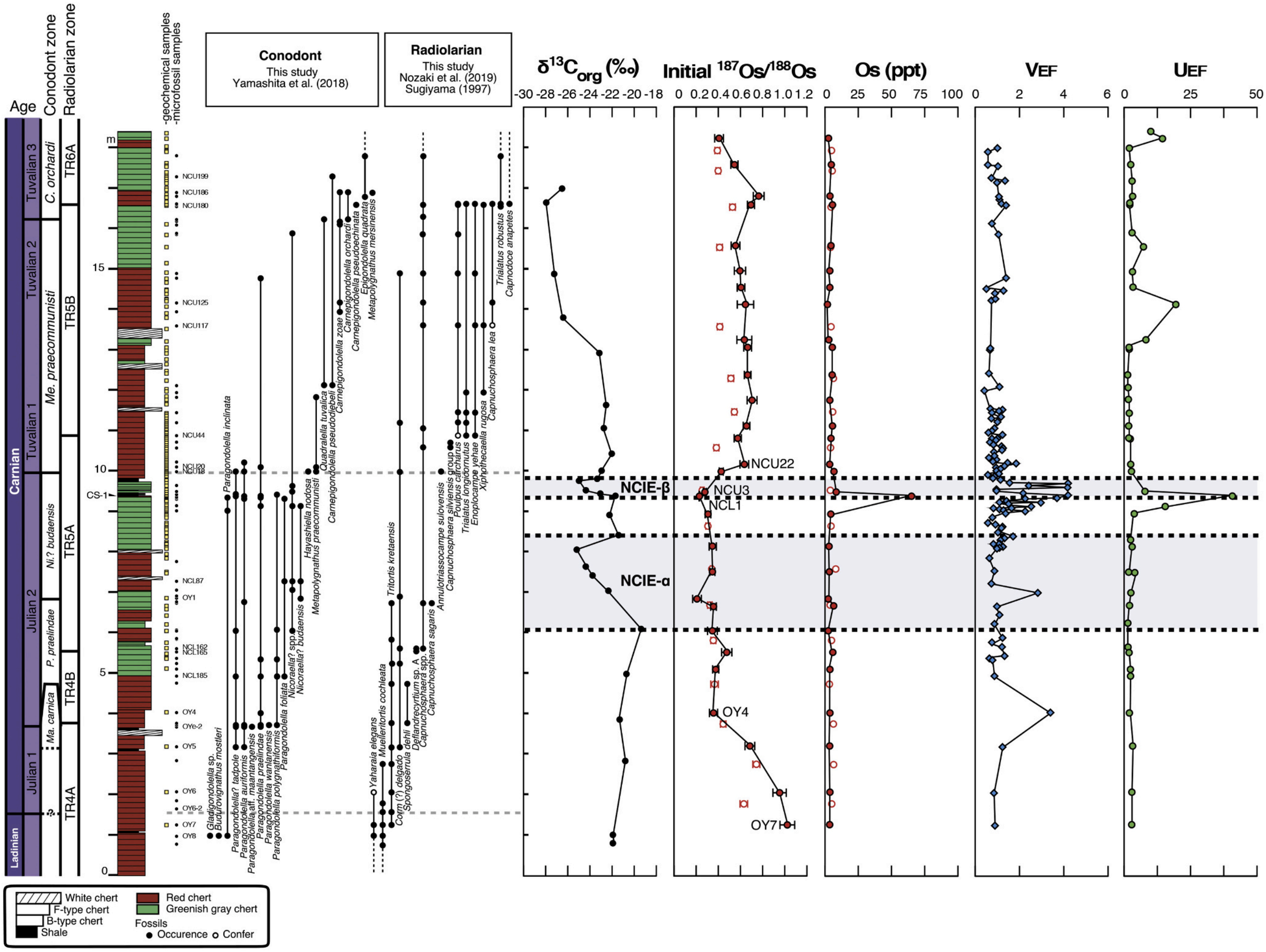

Fig. 3. Stratigraphic profiles of organic carbon isotopes ($\delta^{13}C_{org}$), initial osmium isotope ratios ($^{187}Os/^{188}Os_i$; $t = 230$ Ma), Os concentrations, and enrichment factors for V (V_{EF}) and U (U_{EF}). The shaded areas indicate the two negative carbon isotope excursions (NCIE-α and -β) detected in the study section. The red circles represent Os isotope data reported by Nozaki et al. (2019). The biostratigraphy of conodonts and radiolarians from Sections N—O are also shown. Abbreviations: *Ma.* = *Mazzaella*, *P.* = *Paragondolella*, *Ni.*? = *Nicoraella*, *Me.* = *Metapolygnathus*, and *C.* = *Carnepigondolella.* (For interpretation of the references to colour in this figure legend, the reader is referred to the web version of this article.)

Five radiolarian biozones have been recognized in Section N–O: TR4A = *Muelleritortis cochleata* Zone; TR4B = *Spongoserrula dehli* Zone; TR5A = *Capnuchosphaera* Zone; TR5B = *Poulpus carcharus* Zone; TR6A = *Capnodoce–Trialatus* Zone (in ascending order; Sugiyama, 1997; Nozaki et al., 2019). Sugiyama (1997) correlated the interval from the upper part of the TR4B Zone to the lower part of the TR6A Zone as being the late Ladinian to late Carnian. The TR5A, TR5B, and TR6A zones are calibrated based on the co-occurrence of conodont species from the Inuyama area (Yamashita et al., 2018). Based on conodont data, the TR5A, TR5B, and TR6A zones are correlated to the lower Carnian (Julian), upper Carnian (Tuvalian), and interval from the upper Carnian to middle Norian, respectively.

3. Material and methods

3.1. Conodont and radiolarian biostratigraphy

Fifty-nine chert samples from Section N—O were crushed into small fragments and placed in a 5%–10% HF solution for half a day. The residue was collected with 63 μm and 2 mm sieves. This process was repeated >10 times to collect enough conodont elements and radiolarians. The specimens were handpicked under a binocular microscope, mounted on brass stubs, and digitally photographed with a scanning electron microscope (HITACHI TM3030Plus at Kyushu University, Fukuoka, Japan).

3.2. Sample preparation for geochemical analysis

We collected a total of 183 chert and 50 siliceous claystone samples for whole-rock geochemical analysis. Each sample was crushed and handpicked to avoid contamination from veins and strongly recrystallized/weathered materials. Samples were washed by ultrasonic cleaning in Milli-Q deionized water (>18 MΩ cm). The samples for major (166 chert samples) and trace (46 chert samples) element analysis were finely crushed using a Multi-Beads Shocker (PV1001; Yasui Kikai, Japan), whereas samples for Re—Os (31 chert samples) and carbon (24 siliceous claystone samples) isotope analysis were pulverized in an agate mortar and a ball mill.

3.3. Carbon isotope analysis

Before analysis, all glassware was baked for 2 h at 450 °C, and all tools were cleaned with methanol between use to avoid organic carbon contamination. Approximately 0.6 g of each powdered sample was treated with an excess of 6 M HCl at 40° for 48 h to completely dissolve carbonate minerals. Samples were then rinsed five to six times with

Milli-Q deionized water and dried. Carbon isotope ratios and contents were measured using an elemental analyzer (Fisons Instruments; NA 1500 NCS) coupled to a stable isotope mass spectrometer (Thermo Fisher Scientific; DELTAplusXL) at Kyushu University. The C contents and $\delta^{13}C_{org}$ values were calibrated with a laboratory acetoanillide standard. All isotopic results are reported in conventional delta (δ) notation, defined as per mil (‰) deviations from the Vienna Pee Dee Belemnite (V-PDB) standard.

3.4. *Re and Os isotope analysis*

Re and Os concentrations and isotope ratios were determined by the isotope dilution method using a multi-collector Inductively Coupled Plasma Mass Spectrometry (MC-ICP-MS; Thermo Fisher Scientific NEPTUNE) at JAMSTEC, Yokosuka, Japan. Approximately 2.5 g of powdered sample was weighed, spiked with ^{185}Re and ^{190}Os, and digested in 4 mL of inverse aqua regia in a Carius tube at 220 °C for 24 h. After cooling, the Carius tube was opened and the solution transferred to a Teflon vial into with 9 to 10 mL of Milli-Q deionized water. JMC Os standard solutions (^{187}Os/^{188}Os = 0.106838 ± 0.000015; Nozaki et al., 2012) that contained 50 pg of total Os were also prepared/measured for each analytical batch to check the accuracy of analyses. The Os isotope ratios were determined by MC-ICP-MS with the sparging introduction of OsO_4 gas molecules into the ICP glass torch (Hassler et al., 2000; Nozaki et al., 2012; Kimura et al., 2014; Tokumaru et al., 2015). The data correction for instrumental mass bias within the MC-ICP-MS and different yields among the four multi-ion counters were conducted using a standard bracketing method with the JMC Os standard solution containing 50 pg of total Os dissolved in the diluted inverse aqua regia. The typical Ar gas flow rate during the Os isotope measurement was 1.2 L/min, which is 40 to 50 times higher than the volume of Teflon vials containing the sample and standard solutions. In this case, the memory effect due to the previous sample was quickly removed by the Ar gas flushing with less than 30 s. The error in the Os isotope was calculated assuming that the ion intensity decay during the measurement with the sparging method is subjected to the Poisson distribution (see Nozaki et al., 2012). After the Os measurement, the sample solutions were evaporated on a hotplate at 140 °C to remove the remaining Os. Rhenium was separated from solution using Muromac AG 1-X8 anion exchange resin (Morgan et al., 1991). Rhenium isotope ratios were measured by MC-ICP-MS with a conventional solution introduction system comprising a Scott-type spray chamber and micro-flow nebulizer. Rhenium blanks were 1.84, 18.46 and 3.51 pg, and Os blanks were 0.56, 0.07 and 0.12 pg, respectively, with ^{187}Os/^{188}Os ratio of ~0.167. It should be noted that Re blank of the second analytical batch was abnormally high due to the too long heating and complete dryness of the sample solutions during preparation procedures, inducing some Re volatilization and/or loss (i.e. “apparent” high Re blank). The initial ^{187}Os/^{188}Os ratios of the chert samples were calculated using the sample's estimated age based on biostratigraphy and the astronomically tuned geomagnetic polarity time scale and the ^{187}Re decay constant of 1.666×10^{-11} yr $^{-1}$ (Smoliar et al., 1996). The age correction to calculate initial ^{187}Os/^{188}Os ratios changed the present ^{187}Os/^{188}Os ratios in typically 8.6% (0.8%–36.9%), owing to the low ^{187}Re/^{188}Os ratio of the chert samples. Although the accuracy of the Re concentration may not be good due to the high fraction of the Re blank (Supplementary Table S2), it does not affect the direction of our discussion.

We used an age of 230 Ma for all of the age corrections to the Os isotope data. Although the chert succession investigated in this study ranges in age from the end of the Ladinian (ca. 237 Ma) to the late Carnian (ca. 221 or 228.4 Ma), differences in ^{187}Os/^{188}Os$_i$ values between 237 and 221 (or 228.4) Ma are typically smaller than 0.01 (<3%). As such, the uncertainty associated with the age of the sediments is negligible.

3.5. *Major and trace element analysis*

Major element (Si, Ti, Al, Fe, Mn, Mg, Ca, Na, K, and P) and V, Ni, Cu, and Zn concentrations were determined with an energy dispersive X-ray fluorescence (XRF) spectrometer using a PANalytical Epsilon 3^{XLE} instrument with a Mo X-ray tube at Kyushu University. Powdered samples were oven-dried at 110 °C for 2 h and then mixed with a binder (cellulose) at a ratio of 5:1 (2.0 g of sample to 0.4 g of binder). The mixture was finely homogenized using a Multi-Beads Shocker and pressed at 20 t for 3 min to form a pressed powder pellet. Analyses were calibrated using 22 standard rock samples issued by the Geological Survey of Japan. Detection limits for trace elements were 9 ppm for V, 3 ppm for Ni, and 2 ppm for Cu and Zn. Reproducibility based on the replicate analysis of two standards (JSd-1 and JCh-1) was better than ±1% for Al, Mn, Na, V, Ni, Cu, and Zn, ±3% for Ti, Ca, and K, and ± 10% for P.

Trace element analysis was conducted using an inductively coupled plasma quadrupole mass spectrometer (ICP-QMS; Agilent 7500ce) at JAMSTEC. Powdered samples were dissolved in a HNO_3–$HClO_4$–HF mixture in Teflon vials, and then heated overnight on a hot plate at 110 °C. The digested samples were progressively evaporated at 110 °C for 12 h, 130 °C for 3 h, and 160 °C until dryness. After mixed acid digestion and drying, the remaining sample solution (several drops) was dissolved again in 4 mL of 68% m/m HNO_3, 1 mL of 30% m/m HCl, and 5 mL of Milli-Q deionized water, then heated at 110 °C. Subsequently, there was no residue in the final solutions. Details of the ICP-QMS analytical procedure are given in Takaya et al. (2018).

4. Results

4.1. *Radiolarian biostratigraphy*

In our biostratigraphic analyses, six radiolarian species were newly identified in addition to the 21 species already reported from Section N—O (Sugiyama, 1997; Nozaki et al., 2019). The newly identified species in this study are *Laxtorum* (?) *carnicus* Sugiyama, *Trialatus* cf. *megacornutus* Yeh, *Annulotriassocample sulovensis* Kozur and Mock, *Spinotriassocampe longobardica* Kozur and Mostler, *Silicarmiger latus* Kozur and Mostler, and *Yeharaia elegans* Nakaseko and Nishimura (Figs. 4 and 5). Based on the occurrence of these radiolarian species, five radiolarian biozones established by Sugiyama (1997) were recognized in Section N–O: the TR4A (*Muelleritortis cochleata*), TR4B (*Spongoserrula dehli*), TR5A (*Capnuchosphaera*), TR5B (*Poulpus carcharus*), and TR6A (*Capnodoce–Trialatus*) zones (in ascending order; Fig. 3). The bases of the TR4A, TR4B, and TR5B zones are defined by the first appearance of *Muelleritortis cochleata* (Nakaseko and Nishimura), *Spongoserrula dehli* Cordey et al., and *Poulpus carcharus* Sugiyama, respectively. The bases of the TR5A and TR6A zones are defined by the first appearance of the genus *Capnuchosphaera* De Wever and *Capnodoce* De Wever, respectively.

The lower part of Section N—O (0 to 3.8 m) is correlated to the TR4A Zone of Sugiyama (1997) by the presence of common *Muelleritortis cochleata* and a relatively small number of *Tritortis kretaensis*. According to Sugiyama (1997), *T. kretaensis* is much more abundant than *M. cochleata* throughout the upper part of TR4A. Our biostratigraphic analysis of the studied section also showed that the stratigraphic interval above 1.5 m in the TR4A Zone is characterized by the clear dominance of *T. kretaensis* over *M. cochleata*. Based on the co-occurrence of conodonts and ammonoids in Europe and Turkey, the base of the *T. kretaensis* dominant interval can be correlated with the Ladinian–Carnian boundary (Kozur and Mostler, 1994; Tekin, 1999). Following these studies, we identified the base of the Carnian at the lowest level of the *T. kretaensis* dominant interval within the TR4A Zone.

The stratigraphic interval from 3.8 to 5.4 m in Section N—O can be identified as the TR4B Zone based on the occurrences of *Spongoserrula dehli* (Fig. 3). The base of the TR5A Zone is defined by the first occurrence (FO) of the genus *Capnuchosphaera*, and its top is defined by the FO

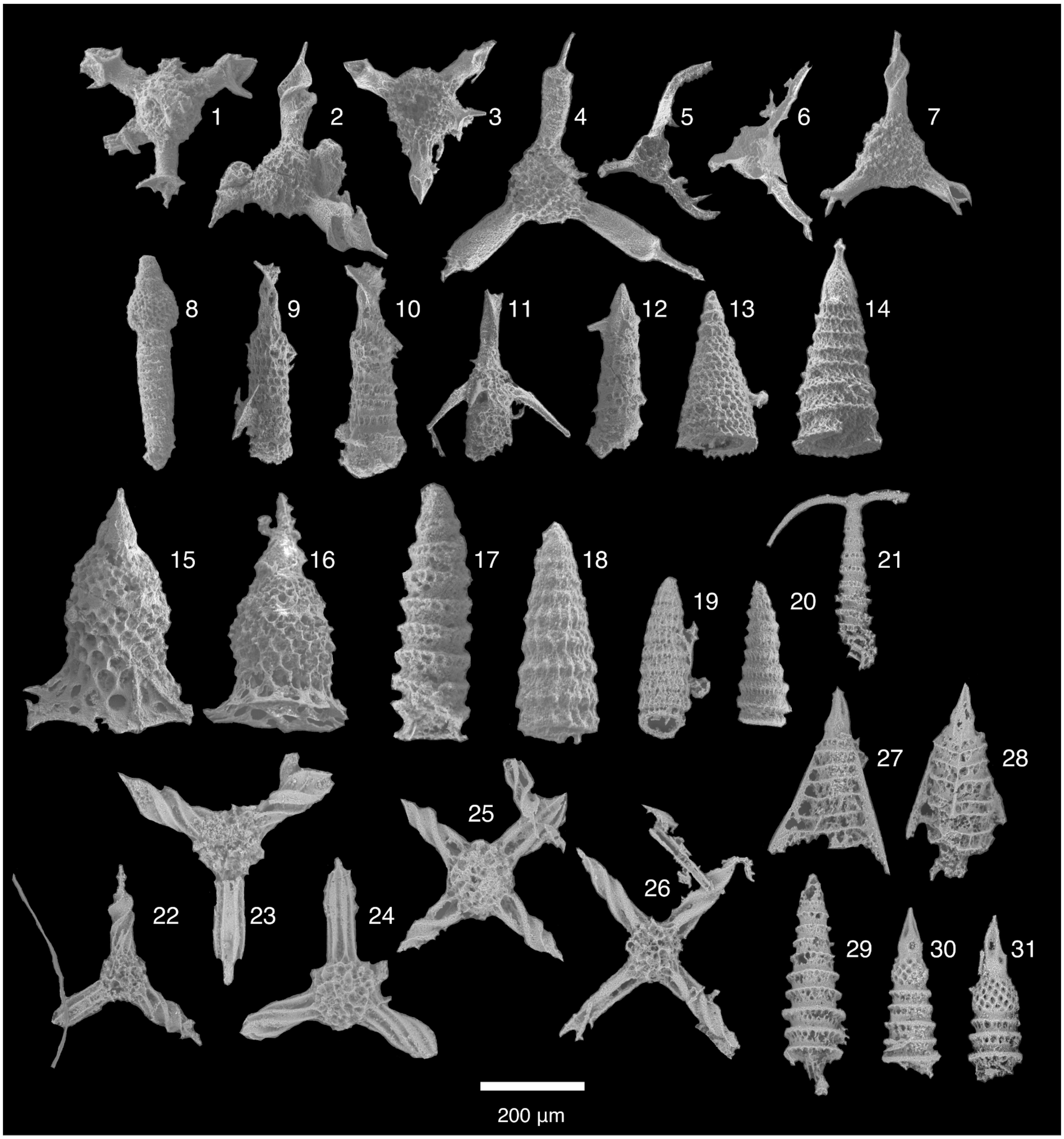

Fig. 4. Middle to Late Triassic radiolarian fossils from the study Section. 1. *Capnuchosphaera tricornis* De Wever in NCU117; 2. *Capnuchosphaera triassica* De Wever in NCU117; 3. *Capnuchosphaera* sp. in NCU44; 4. *Capnuchosphaera lea* De Wever in NCU117; 5. *Poulpus carcharus* Sugiyama in NCU186; 6. *Poulpus* cf. *carcharus* Sugiyama in NCU44; 7. *Capnuchosphaera* sp. in NCL162; 8. *Xiphothecaella rugosa* Bragin in NCU180; 9, 10. *Trialatus* cf. *megacornutus* Yeh in NCU117 and NCU125; 11. *Trialatus longocornutus* Yeh in NCU44; 12. *Enoplocampe yehae* Sugiyama in NCU117; 13. *Laxorum* (?) *carnicum* Sugiyama in NCU117; 14. *Multimonilis japonicus* Sugiyama in NCU180; 15, 16. *Deflandrecyrtium* sp. A in NCL162 and NCL165; 17. *Annulotriassocampe sulovensis* Kozur and Mock in NCU18; 18. *Corum* (?) *delgado* Sugiyama in NCU12; 19. *Corum* (?) sp. in OY5; 20. *Triassocampe* sp. in NCU117; 21. *Spinotriassocampe longobardica* Kozur and Mostler in OY7; 22–24. *Tritortis kretaensis* Kozur and Krahl in OY5, OY6-2; 25, 26. *Muelleritortis cochleata* Nakazawa and Nishimura in OY6 and OY8; 27, 28. *Silicarmiger latus* Kozur and Mostler in OY7 and OY8; 29. *Triassocampe postdeweveri* Kozur and Mostler in OY7; 30, 31. *Yaharaia elegans* Nakaseko and Nishimura group in OY7 and OY8.

of *Poulpus carcharus* (Sugiyama, 1997). The samples in the middle part of Section N—O (5.4 to 10.9 m) yield *Capnuchosphaera silviensis* group, *C. sagaris*, *Capnuchosphaera* spp., *Deflandrecyrtium* sp. A, and *Annulotriassocampe sulovensis* (Fig. 3). This faunal assemblage is comparable to the TR5A Zone.

The stratigraphic interval between 10.9 and 16.5 m was correlated with the TR5B Zone by Nozaki et al. (2019). Our biostratigraphic analysis confirmed that the radiolarian species in this interval characterize the TR5B Zone, including *P. carcharus*, *Trialatus longicornutus*, *T. megacornutus*, *Enoplocampe yehae*, *C. tricornis*, *C. lea*, and *Xiphothecaella rugosa*. The uppermost part of Section N—O corresponds to the TR6A Zone, which is supported by the occurrence of *C. anapetes* and *T. robustus* (Fig. 5).

4.2. Conodont biostratigraphy

Conodonts are hard to find at the base of the Carnian in the studied section. However, we collected 18 conodont species in 28 of 55 chert samples from above the 3.0 m level, and identified 7 conodont genera: *Budurovignathus*, *Carnepigondolella*, *Gladigondolella*, *Hayashiella*,

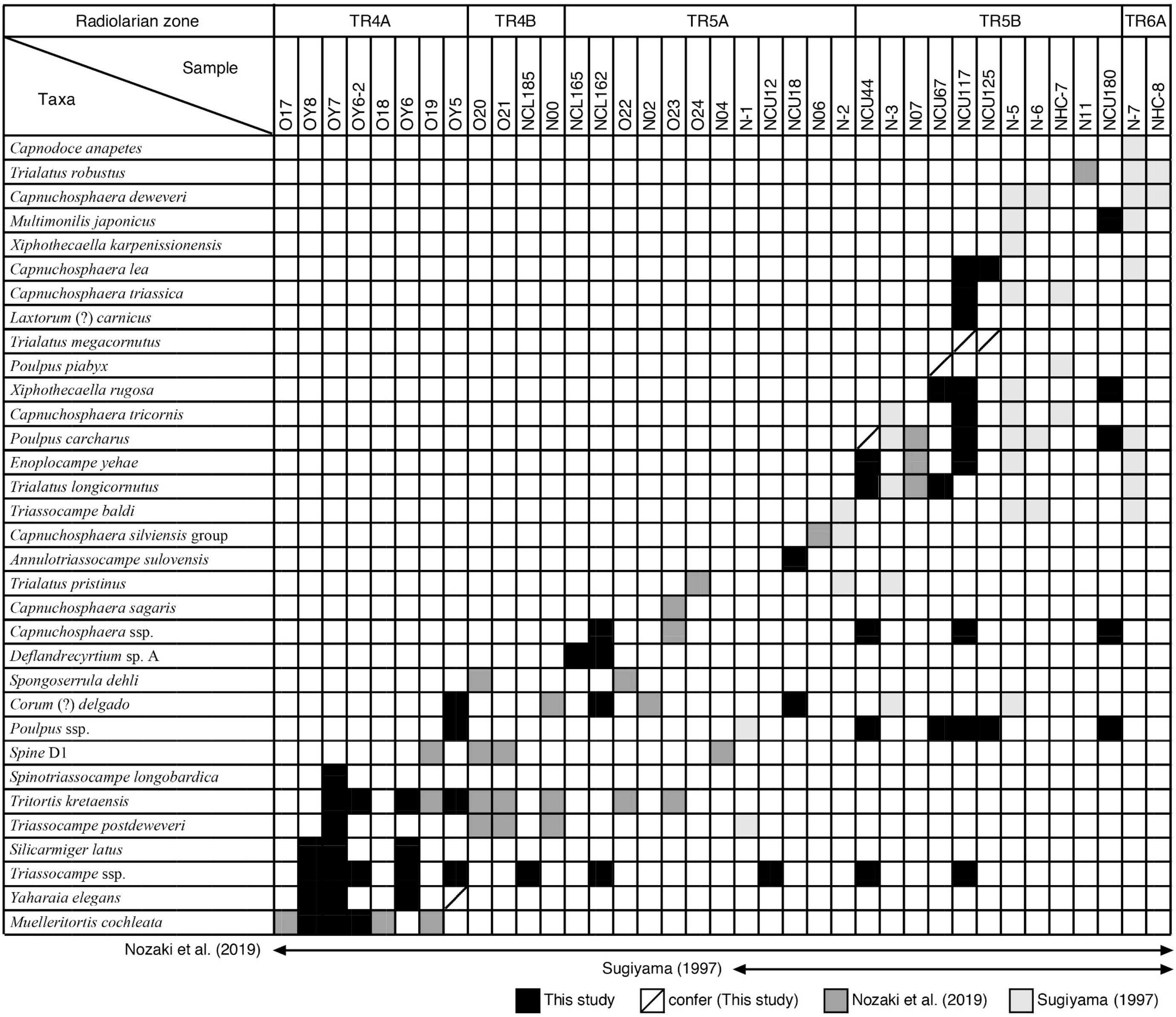

Fig. 5. List of radiolarian fossils from Sections N—O. The stratigraphic levels of samples are shown in Fig. 3 and Supplementary Table S3.

Metapolygnathus, *Nicoraella?*, and *Paragondolella* (Figs. 6 and 7).

In the lowest part of the section, we found *Gladigondolella* sp., *Budurovignathus mostleri* and *Paragondolella inclinata* in sample OY8 (Fig. 3). The stratigraphic ranges of *B. mostleri* and *P. inclinata* are from the upper Ladinian (Longobardian) to the lowermost Carnian and the Ladinian to upper part of the upper Carnian, respectively (Kozur et al., 1994; Rigo et al., 2007, 2018). This association is in agreement with the radiolarian biostratigraphic investigation that identified the base of the Carnian at the stratigraphic interval of ca. 1.5 m, assigning a late Ladinian age to the conodont sample OY8.

Successively, the following five conodont biozones proposed by Rigo et al. (2018) were established based on the FO and age ranges of diagnostic species in the studied section: *Mazzaella carnica*, *Paragondolella praelindae*, *Nicoraella*? *budaensis*, *Metapolygnathus praecommunisti*, and *Carnepigondolella orchardi* Zones (in ascending order; Fig. 3). The conodont distribution in the studied section reflects the global distribution of conodonts during this interval. Most Upper Triassic conodont research has considered rocks deposited in western Tethys (Europe), eastern Tethys (China), and North America (Canada), and our study provides documentation for mid-Panthalassa conodonts. The documentation of the same conodont associations in the Tethys and in mid-Panthalassa oceans confirms that most of the Upper Triassic conodonts were cosmopolitan, and allowed the Tethyan biozones to be extended to other geographic areas/domains (Rigo et al., 2018). On this basis, we applied the conodont biozonation proposed for the Tethys Ocean by Rigo et al. (2018) to our studied section. In particular, the proposed biozones from Rigo et al. (2018) are interval zones, the base of which are placed with the FO of the index species. In addition, the three turnovers (T1, T2, T3) first described from the upper Carnian Pizzo Mondello section (Sicily, Italy), one of the two GSSP (Global Stratotype Section and Point) candidate sections for the base of the Norian, have been recently identified in the other GSSP candidate section, the Black Bear Ridge section in British Columbia (Canada) (Orchard, 2019). The widespread nature of these biozones suggests a global distribution for the Carnian conodont associations, since the two candidate GSSP sections were located on opposite sides of Pangea. Some of the Late Triassic conodont taxa may be endemic to certain oceans; e.g. members of the genus *Acuminatella*, which have only been documented in North America, or the genus *Neocavitella*, which has only been found in the Tethys Ocean. A taxon once thought to be endemic is *Ni.*? *budaensis*, described

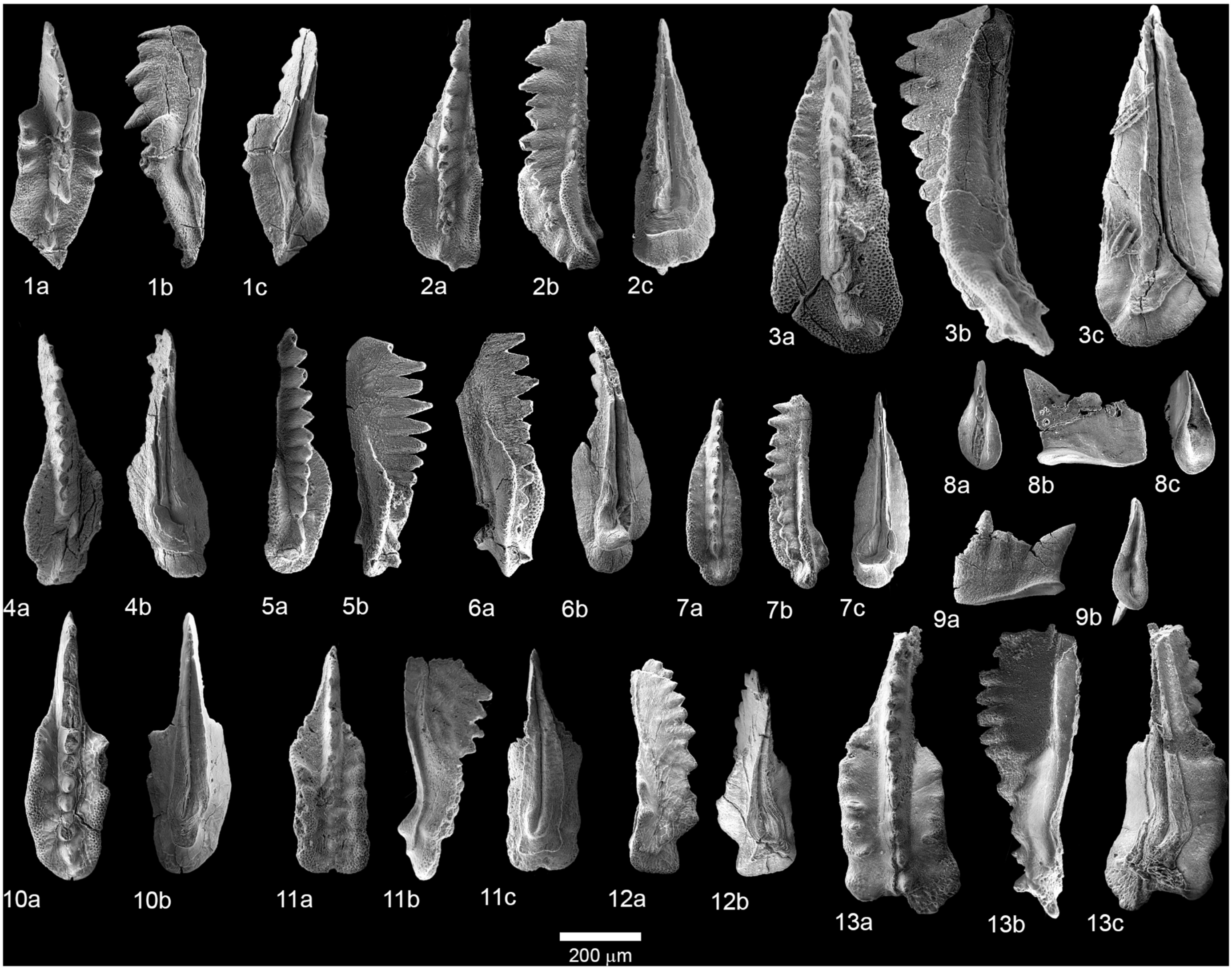

Fig. 6. Middle to Late Triassic conodont fossils from the study Section. 1. *Budurovignathus mostleri* Kozur in OY8; 2. *Paragondolella auriformis* Kovács in OY5; 3. *Paragondolella maantangensis* Dai and Tian in OY2-e; 4. *Paragondolella praelindae* Kozur in OY2-e; 5. *Paragondolella*? *tadpole* Hayashi in OY2-e; 6, 7. *Paragondolella praelindae* Kozur in OY-e and NCL185; 8, 9. *Nicoraella? budaensis* Kozur and Mock in OY1 and NCL87; 10. *Metapolygnathus praecommunisti* Mazza in NCU20; 11. *Carnepigondolella zoae* Orchard in NCU125; 12. *Carnepigondolella orchardi* Kozur in NCU186; 13. *Carnepigondolella pseudodiebeli* Kozur in NCU199. For 1–20: a = upper view; b = lateral view; c = lower view.

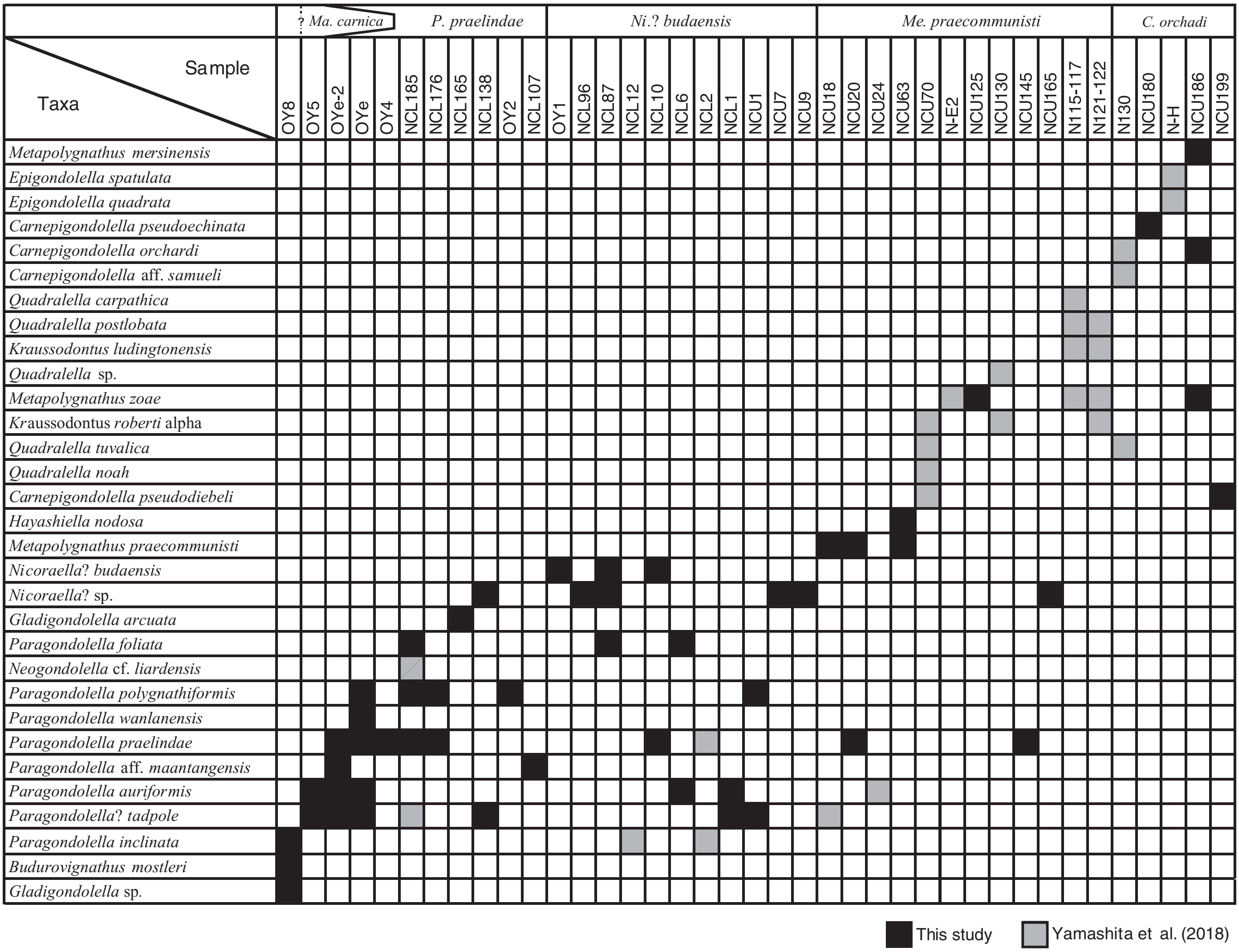

		? *Ma. carnica*				*P. praelindae*						*Ni.? budaensis*											*Me. praecommunisti*												*C. orchadi*				
Sample Taxa	OY8	OY5	OYe-2	OYe	OY4	NCL185	NCL176	NCL165	NCL138	OY2	NCL107	OY1	NCL96	NCL87	NCL12	NCL10	NCL6	NCL2	NCL1	NCU1	NCU7	NCU9	NCU18	NCU20	NCU24	NCU63	NCU70	N-E2	NCU125	NCU130	NCU145	NCU165	N115-117	N121-122	N130	NCU180	N-H	NCU186	NCU199
Metapolygnathus mersinensis																																						■	
Epigondolella spatulata																																					▒		
Epigondolella quadrata																																					▒		
Carnepigondolella pseudoechinata																																				■			
Carnepigondolella orchardi																																			▒			■	
Carnepigondolella aff. *samueli*																																			▒				
Quadralella carpathica																																	▒						
Quadralella postlobata																																	▒	▒					
Kraussodontus ludingtonensis																																	▒	▒					
Quadralella sp.																														▒									
Metapolygnathus zoae																												▒	■				▒	▒				■	
*K*raussodontus *roberti* alpha																											▒			▒				▒					
Quadralella tuvalica																											▒								▒				
Quadralella noah																											▒												
Carnepigondolella pseudodiebeli																											▒												■
Hayashiella nodosa																										■													
Metapolygnathus praecommunisti																							■	■		■													
Nicoraella? budaensis												■		■		■																							
Nicoraella? sp.									■				■	■							■	■										■							
Gladigondolella arcuata								■																															
Paragondolella foliata						■								■			■																						
Neogondolella cf. *liardensis*						▒																																	
Paragondolella polygnathiformis				■		■	■			■										■																			
Paragondolella wanlanensis				■																																			
Paragondolella praelindae			■	■	■	■	■									■		▒						■							■								
Paragondolella aff. *maantangensis*			■								■																												
Paragondolella auriformis		■	■	■													■		■						▒														
Paragondolella? tadpole		■	■	■		▒			■										■	■			▒																
Paragondolella inclinata	■														▒			▒																					
Budurovignathus mostleri	■																																						
Gladigondolella sp.	■																																						

■ This study ▒ Yamashita et al. (2018)

Fig. 7. List of conodont fossils from Sections N—O. The stratigraphic levels of samples are shown in Fig. 3 and Supplementary Table S3.

from an apparently restricted basin in pelagic cherty limestones from Slovenia (Kolar-Jurkovšek et al., 2005) but was recently documented in rocks from the mid-Panthalassic Ocean, where it is found in association with various species of the genus *Paragondolella*, including *P. praelindae*, the most common conodont recorded during the Carnain Pluvial Episode. It is thus possible to extend the Tethyan biozonation to the mid-Panthalassa, at least for the Carnian.

4.2.1. *Mazzaela carnica Zone*

Difinition.—The lower boundary is marked by the FO of the index species *Mazzaela carnica.*

Although *Ma. carnica* has not been found in the studied section, it is possible to approximate its stratigraphic range with the distribution of *Paragondolella auriformis* (Rigo et al., 2007, 2018). *Ma. carnica* and *P. auriformis* have similar ranges, except for the somewhat early first occurrence of *P. auriformis.* The age of this association, is uppermost Julian 1, and it corresponds to the uppermost *Trachyceras aon* ammonoid Zone and *T. aonoides* Zone.

4.2.2. *Paragondolella praelindae Zone*

Difinition.— The base of this zone is defined by the FO of *Paragondolella praelindae.*

This zone is characterized by the occurrence of *P. praelindae* with *P.? tadpole*, *P. auriformis,* and *P. polygnathiformis*. Such a *Paragondolella* assemblage indicates that this zone is correlative to the *P. praelindae* Zone in Tethyan sections (Rigo et al., 2018). The *P. praelindae* Zone is dated to the late Julian substage (Julian 2), based on the co-occurrence of the ammonoid species of the *Austrotrachyceras austriacum* Zone in Tethyan sections (Mietto et al., 2012; Rigo et al., 2007, 2012). Thus, the base of the *P. praelindae* Zone in the studied section is correlated to the base of the Julian 2.

4.2.3. *Nicoraella? budaensis Zone*

Difinition.—The lower boundary of this zone is defined by the FO of *Nicoraella*? *budaensis*.

Ni.? *budaensis* occurs with *P. foliata* and *P. praelindae* in this interval. *Ni.*? *budaensis* has a limited geographic distribution, and has been previously reported only from Europe (Slovenia, Hungary, and Italy; Kozur and Mock, 1991; Kolar-Jurkovšek et al., 2005). Although the entire stratigraphic range of *Ni.*? *budaensis* within the Carnian is not precisely known, *Ni.*? *budaensis* occurs from the upper Julian to Julian–Tuvalian boundary in the Tethys realm (e.g. Kozur and Mock, 1991; Kolar-Jurkovšek et al., 2005; Kolar-Jurkovšek and Jurkovšek, 2010; Rigo et al., 2018).

4.2.4. *Metapolygnathus praecommunisti Zone*

Difinition.—The base of this zone is defined by the FO of *Metapolygnathus praecommunisti*.

The co-occurrences of *Metapolygnathus praecommunisti* with *Hayashiella tuvalica, H. nodosa*, and *Carnepigondolella zoae* suggest this zone is clearly comparable with the Tethyan *Me. praecommunisti* Zone of Rigo et al. (2018). The *Me. praecommunisti* Zone in the Tethys corresponds with the ammonoid *Tropites dilleri* Zone to the *Anatropites spinosus* Zone (Balini et al., 2010), and the stratigraphic range of *Me. praecommunisti* is from the lower Tuvalian (Tuvalian 1) to upper Tuvalian (Tuvalian 3) (Mazza et al., 2011). Thus, the base of the *Me. praecommunisti* Zone in the studied section is correlated to the base of the Tuvalian.

4.2.5. *Carnepigondolella orchardi* Zone

Difinition.—The uppermost part of Section N—O (16.2 to 18.4 m) is correlated to the *Carnepigondolella orchardi* Zone of Rigo et al. (2018), which is defined by the FO of *C. orchardi.*

This zone is also characterized by the FO of *C. pseudoechinata* and *Me. mersinensis* in the studied section. The *C. orchardi* Zone can be correlated with the lower *Anatropites spinosus* ammonoid Zone, which indicates a latest Tuvalian (Tuvalian 3) age (Balini et al., 2012; Rigo et al., 2018). Based on this comparison, the base of our *C. orchardi* Zone can be correlated with the base of the Tuvalian 3.

4.3. Organic carbon isotopes

$\delta^{13}C_{org}$ values range from −27.9‰ to −19.4‰ in the studied section (Supplementary Table S1). In the basal ~6 m of Section N—O, $\delta^{13}C_{org}$ values are slightly increased from −21.9‰ to −19.4‰ (average = −21.0‰) (Fig. 3). In the middle Julian 2, the first negative $\delta^{13}C_{org}$ excursion (here designated as NCIE-α) is observed (ca. 5.8‰ drop from −19.4‰ to −25.2‰). The $\delta^{13}C_{org}$ values then increase rapidly upwards, and are constant below the CS-1 siliceous claystone (average = −21.8‰). Above the CS-1 siliceous claystone, $\delta^{13}C_{org}$ values again decrease abruptly from −21.7‰ to −25.0‰ (ca. 3.3‰ drop). The stratigraphic age of this second negative $\delta^{13}C_{org}$ excursion (NCIE-β) is correlated to the uppermost part of the Julian 2. In the Tuvalian 1 to 3, $\delta^{13}C_{org}$ values gradually decrease from −22.0‰ to −27.9‰.

4.4. Re and Os isotopes

Concentrations of Re and Os in the chert samples are 0.68–34.1 and 0.760–67.1 ppt, respectively (Supplementary Table S2). Sample NCL1 and NCL1-2, just below the CS-1 siliceous claystone in Section N—O, have the highest total Os concentration (63.4 and 67.1 ppt), which is two times higher than that of average upper continental crust (UCC; Os = 31 ppt; Peucker-Ehrenbrink and Jahn, 2001). Os concentrations in the Sakahogi cherts are relatively constant (2.7 ± 1.4 ppt; average ± 1SD; n = 29), except for two samples with much higher Os concentrations (NCL1 and NCL1-2). (Fig. 3).

Initial Os isotope ratios ($^{187}Os/^{188}Os_i$) during the Julian 1 gradually decrease from 1.02 to 0.356 (OY7 to OY4; Fig. 3). The samples in the Julian 2 are characterized by relatively constant and unradiogenic initial Os isotope ratios between 0.231 and 0.474 (average = 0.323 from OY4 to NCL1). Initial Os isotope ratios gradually increase across the Julian–Tuvalian boundary from 0.282 to 0.627 (NCU3 to NCU22), and then become steady (0.410–0.760) in the Tuvalian.

4.5. Redox-sensitive elements

Abundances of the redox-sensitive elements, such as U and Mo, show a negative correlation with SiO_2. This is attributed to dilution with nearly pure biogenic silica (e.g. radiolarians) in the chert samples (Hori et al., 1993; Takiguchi et al., 2006; Sato et al., 2013). To avoid the significant dilution effect by biogenic SiO_2, reflecting fluctuations in radiolarian test abundances, concentrations of the redox-sensitive elements were normalized using Al concentrations and compared with those of the UCC composition (Rudnick and Gao, 2014) to obtain enrichment factors. The enrichment factor is defined as follows:

$$X_{EF} = \left(X_{sample}/Al_{sample}\right)/(X_{UCC}/Al_{UCC})$$

where X and Al are the weight concentrations of element X and Al, respectively.

The stratigraphic variations of V and U enrichment factors are shown in Fig. 3, and the enrichment factors of other redox-sensitive elements, such as Mo, Ni, Zn, and Cu, are reported in Supplementary Tables S3 and S4. Vanadium, U, and Mo form highly soluble ions under oxygenated conditions, but under anoxic conditions, they are insoluble in their lower valency state (Calvert and Pedersen, 1993, 2007). The V enrichment factor (V_{EF}) increases abruptly from 0.6 to 4.2 in the late Julian 2 (8.9 to 9.8 m depth). Similarly, the U enrichment factor (U_{EF}) increases abruptly from 3.0 to 41.2, with peak values in sample NCL1 (Fig. 3). However, the Mo enrichment factor (Mo_{EF}) is constantly low in the studied section, and there are no stratigraphic variations of Mo_{EF} in the late Julian 2 (Supplementary Table S4).

In addition to the redox-sensitive elements, the enrichment factors of chalcophile elements (e.g. $Ni_{EF,}$ Cu_{EF}, and Zn_{EF}) are also useful tracers for redox conditions, since these elements form highly insoluble sulfides under anoxic and/or euxinic bottom water conditions (Calvert and Pedersen, 1993; Algeo and Maynard, 2004). The enrichment factors of Ni, Cu, and Zn are higher than those of UCC, however, there are no significant changes in these elements in the late Julian 2 (Supplementary Table S3).

5. Discussion

5.1. Carnian marine Os isotopic record

Problems associated with post-depositional modification by Re and Os redistribution during weathering have been discussed in previous studies (e.g. Georgiev et al., 2012). Georgiev et al. (2012) showed that the systematics of Re—Os in black shale samples can effectively discriminate between weathered and fresh shale, even when weathering is subtle and not visible in outcrop, and when weathered shale has the same major and trace element chemistry as the fresh shale. Although we carefully handpicked fresh chert samples to avoid contamination from strongly recrystallized/weathered materials, we cannot completely rule out the possibility of secondary remobilization of Re and Os. However, we consider that the Re—Os isotopic disturbance in the studied chert samples from Section N—O is minor, as secondary remobilization of Re and Os was not observed at the middle Norian ejecta layer, which is located ~20 m west of the study section (Onoue et al., 2012; Sato et al., 2013). Sato et al. (2013) showed that there is no evidence of remobilization of Re and Os from the ejecta layer, which had higher Re and Os contents (~0.11 ppb Re and ~ 3.1 ppb Os) than the adjacent chert layers (12–16 ppt Re and 6–11 ppt Os).

Our study reveals that Os isotope ratios during the Julian are characterized by: (1) a continuous decrease in the Julian 1; (2 low values during the Julian 2; and (3) an abrupt increase at the end of the Julian 2. The conspicuous decrease in $^{187}Os/^{188}Os_i$ ratios may be explained by: (1) a decrease in the flux of radiogenic Os from riverine water (continental weathering); (2) extraterrestrial impacts; or (3) a large and prolonged input from a comparatively unradiogenic Os volcanic source (e.g. Peucker-Ehrenbrink and Ravizza, 2000, 2012). A rapid decline in riverine water flux is unlikely, because sedimentological and palynological studies clearly show that a humid pulse occurred at the base of the Julian 2 and ended in the early Tuvalian (Simms and Ruffell, 1989, 1990; Roghi et al., 2010; Mueller et al., 2016). It can also not be explained by an extraterrestrial impact, which would have produced an abrupt $^{187}Os/^{188}Os_i$ ratio decline followed by a rapid recovery, as observed in the pelagic deposits from the middle Norian (Sato et al., 2013), late Eocene (Paquay et al., 2008), and Cretaceous–Paleogene boundary (Ravizza and Peucker-Ehrenbrink, 2003; Robinson et al., 2009). Moreover, no large impact event has been identified in the Carnian (Schmieder and Kring, 2020).

Given that the decline in $^{187}Os/^{188}Os_i$ ratios to highly unradiogenic values (~0.2) continued for at least a few million years during the Julian (ca. 237–232 or 233.5 Ma; Ogg, 2012) (Fig. 3), prolonged volcanic activity is the most plausible mechanism to explain the Os isotopic record. Although the possibility cannot be excluded that we couldn't determine high ^{187}Os/^{188}Os$_i$ ratios associated with intensive continental weathering or intermittent subsided volcanic activity because of a lower sampling resolution than the residence time of Os, a prolonged interval of low ^{187}Os/^{188}Os$_i$ ratio suggest that the relative fluxes of the major osmium inputs from hydrothermal fluids and riverine water (continental weathering) to oceans remained somewhat steady during the Julian. A similar Myr-scale decrease in ^{187}Os/^{188}Os$_i$ ratios was observed in early Aptian pelagic carbonates from Italy (Tejada et al., 2009) and Rhaetian bedded cherts from Japan (Kuroda et al., 2010). In both cases, a causal relationship was proposed between the observed shift to unradiogenic Os and large-scale mantle upwelling that formed LIPs (Ontong Java Plateau and Central Atlantic Magmatic Province (CAMP), respectively), though the correspondence between the onset of CAMP volcanism and the negative shift toward unradiogenic Os isotope compositions in the early Rhaetian remain debated (Kuroda et al., 2010; Callegaro et al., 2012). As such, a large input of unradiogenic Os from mantle-derived sources is the likely reason for the negative Os isotope shift in the Julian during emplacement of the Wrangellia large igneous province, as discussed below, in Section 5.2.

Nozaki et al. (2019) demonstrated that the variability in the long-term Os isotope record during the Triassic is similar to that of the coeval marine Sr isotope record. The residence time of Os in seawater (several tens of thousands of years; Levasseur et al., 1999) is almost two orders of magnitude shorter than that of Sr (several millions of years; Allègre et al., 2010). Therefore, the Os isotope composition of seawater changes much more rapidly in response to changes in the flux or isotopic composition of the major inputs. A small decline in Sr isotope ratios during the Julian is recognized from Carnian limestones of the western

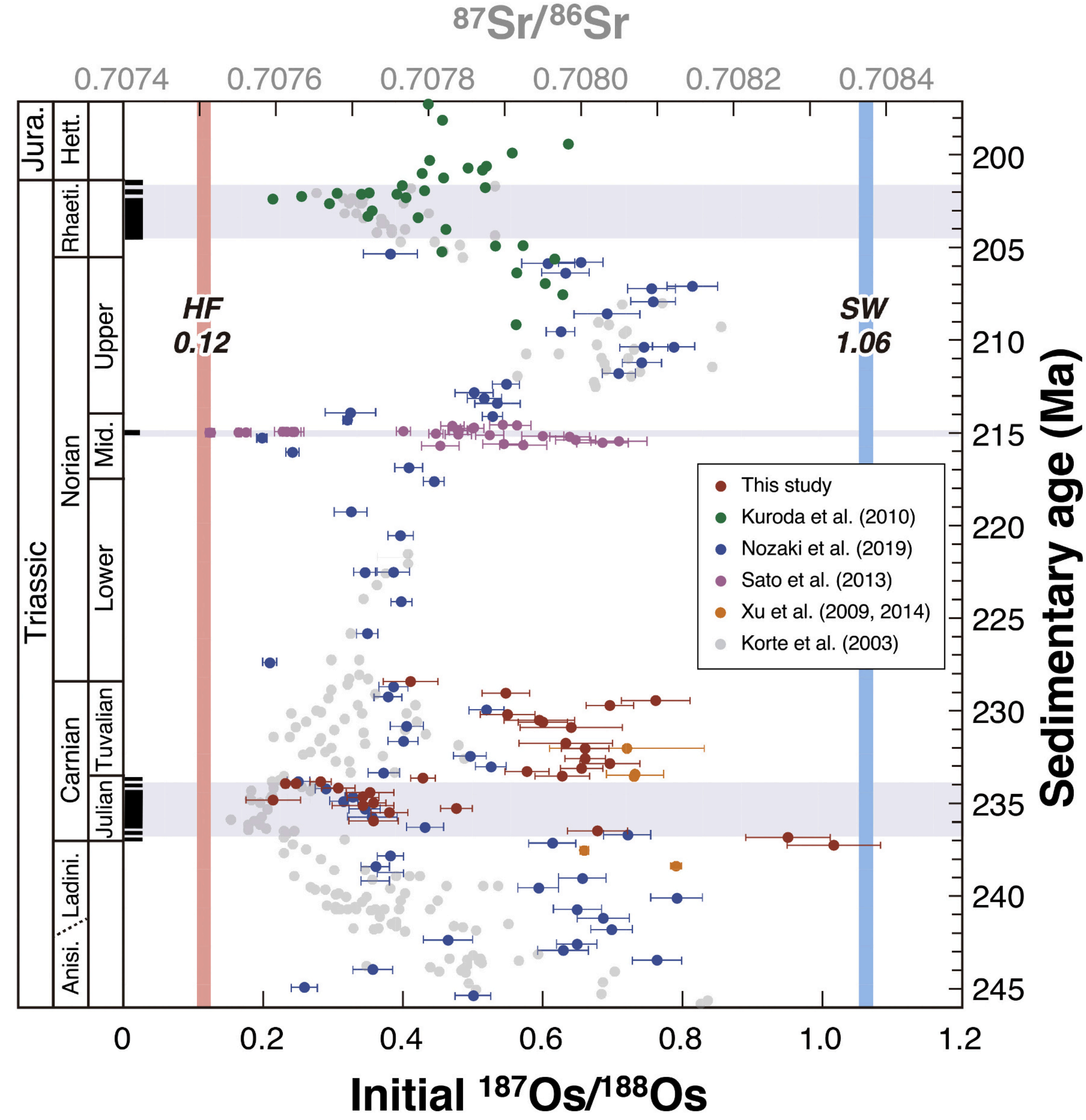

Fig. 8. Stratigraphic profile of initial ^{187}Os/^{188}Os for the Triassic sections (This study; Kuroda et al., 2010; Nozaki et al., 2019; Sato et al., 2013; Xu et al., 2009, 2014), as well as ^{87}Sr/^{86}Sr in the Triassic seawater (Korte et al., 2003). SW = present-day seawater ^{187}Os/^{188}Os ratios; HF = present-day hydrothermal fluid ^{187}Os/^{188}Os ratios. Sedimentary ages are from Nozaki et al. (2019). Errors of this study, Nozaki et al. (2019), Sato et al. (2013) and Xu et al. (2009, 2014) are 2SD, and errors of Kuroda et al. (2010) are 2SE. The gray shaded areas in Julian, middle Norian and Rheatian show the estimated eruption ages of the Wrangellia volcanism, impact ejecta, and CAMP volcanism, respectively.

Tethys (Korte et al., 2003; see also Fig. 8). The Sr and Os isotope curves are different as a result of the differing residence times of Sr and Os in the ocean, and thus the amplitude of the Os isotope record is much larger than that of the Sr isotope record.

Initial Os isotope ratios gradually increase across the Julian–Tuvalian boundary and remain consistent during the Tuvalian (Fig. 3); these radiogenic initial ^{187}Os/^{187}Os ratios (0.4–0.6) persisted from the Tuvalian to the late Norian (Nozaki et al., 2019; Fig. 8). Thus, the period of stable initial ^{187}Os/^{187}Os ratios after the CPE that extends from the Tuvalian to the late Norian suggests these values represent a new steady state.

5.2. *Wrangellia large igneous province*

The eruption of the Wrangellia Flood Basalt (FB) onto the Farallon Plate in the Panthalassa Ocean has been widely known as a large igneous province (LIP) volcanism occurred in the Carnian (Greene et al., 2010). The Wrangellia FB today crops out in northwestern America, from Vancouver Island (Canada) to Alaska (Jones et al., 1977; Greene et al., 2010). Paleomagnetic studies suggest that the Wrangellia basalts were erupted at equatorial latitudes of ca. 10–17°N and accreted to western North America in the Late Jurassic or Early Cretaceous (Jones et al., 1977; Hillhouse and Gromme, 1984; Hampton et al., 2010). The age of the Wrangellia basalts is constrained by bivalves and ammonoids from sedimentary rocks that underlie and overlie the Wrangellia FB. Below the Wrangellia FB sequence, silicified shales contain the bivalve *Daonella*, which suggests a middle Ladinian age (Jones et al., 1977). Above the Wrangellia FB sequences, limestones contain rich ammonoid fauna of the *Tropites dilleri* Zone, indicating an early late Carnian age (Carlisle and Susuki, 1974; Tozer, 1994). Thus, the eruption age of Wrangellia LIP volcanism can be biostratigraphically constrained between the middle Ladinian and early late Carnian (Tuvalian 1).

Our biostratigraphic investigation reveals that low in ^{187}Os/^{188}Os$_i$ ratios throughout the Julian 2 overlaps with the biostratigraphically constrained age of the Wrangellia FB. ^{40}Ar/^{39}Ar and U—Pb ages of the Wrangellia basalts and intrusive rocks are 233–227 Ma (Parrish and McNicoll, 1992; Schmidt and Rogers, 2007; Greene et al., 2010). Despite the uncertainties regarding Carnian chronology (Ogg et al., 2014; Ogg, 2015), the ages of the Wrangellia basalts are in agreement with the U—Pb age of 230.91 ± 0.33 Ma for an Aglianico volcanic ash bed in the Pignola 2 section, southern Italy (Furin et al., 2006), where the CPE is well constrained by conodont and palynomorph biostratigraphy (Rigo et al., 2007, 2012; Mazza et al., 2011) and magnetostratigraphically correlated to the APTS (Maron et al., 2019). The ^{40}Ar/^{39}Ar and U—Pb ages suggest that the eruption of the Wrangellia flood basalts took place after the Tuvalian, which is not consistent with the end of Wrangellia volcanism estimated from the ammonoid occurrences of the *Tropites dilleri* Zone (Tuvalian 1). However, the ^{40}Ar/^{39}Ar age spectra might reflect the widespread alteration of the Wrangellia basalts, and have analytical errors of less than ±10 Myr (Greene et al., 2010), and most of the ^{40}Ar^{39}Ar ages of the Wrangellia basalts have been reset to ages younger than the emplacement age of the LIP (Greene et al., 2010). The two available U—Pb ages measured from baddeleyite and zircons of the Wrangellia basalts (227.3 ± 2.6 and 232.2 ± 1.0 Ma; Mortensen and Hulbert, 1992; Parrish and McNicoll, 1992) are also not very precise, as they were obtained on chemically untreated multi-grain aliquots (Dal Corso et al., 2020).

In addition to the Wrangellia FB, Carnian oceanic basalts of an intraplate origin, including oceanic seamounts and plateaus, have been recognized in the Jurassic accretionary complexes of East Asia (Japan and Far East Russia). These Carnian basalts originated from an open-ocean realm of the Panthalassa Ocean on the Izanagi Plate and were accreted along the East Asian subduction zone during the Late Jurassic–Early Cretaceous (Matsuoka, 1992; Isozaki, 1996; Onoue et al., 2004; Safonova et al., 2015). These typically occur in the Sambosan Belt of Japan (Onoue et al., 2004; Onoue and Sano, 2007; Safonova et al., 2015) and Taukha Belt of Sikhote–Alin Mountains, Far East Russia (Fig. 1A; Kojima, 1989; Faure and Natal'in, 1992; Punina, 1997). The lithologies, accretion ages, and faunal similarities between the Sambosan and Taukha belts (Kojima et al., 2000; Stanley and Onoue, 2015) clearly indicate the extent of the East Asian Jurassic subduction zone for ca. 3000 km. The Carnian oceanic basalts in these accretionary complexes occur as laterally discrete slabs and blocks of various size, and are complexly mingled with terrigenous clastic rocks to form a tectonic mélange (Onoue et al., 2004).

The geochemical features of most of the Sambosan and Taukha basalts are consistent with derivation from a plume-related mantle source in a mid-oceanic location. The basalts are enriched in incompatible elements, especially in high-field-strength elements (e.g. Ti, Zr, and Nb) and light rare earth elements (Ishizuka et al., 2003; Onoue et al., 2004; Safonova, 2009; Safonova et al., 2015). Diverse U—Pb ages (164–456, 724–955, and 1638–2202 Ma) have been reported for Carnian basaltic rocks of the Sambosan Belt, which suggest heterogeneous recycled source components in a mantle plume generated the oceanic basalts (Gao et al., 2018).

The timing of the basaltic volcanism in the Sambosan belt is constrained to be between the Ladinian and late Carnian based on the occurrence of: (1) upper Carnian conodonts from the interpillow, shallow-water and pelagic limestones that overlie the basaltic lavas (Khanchuk et al., 1989; Ishida and Hirsch, 2001; Onoue and Sano, 2007); (2) lower Carnian bivalve assemblage (similar to typical St. Cassian fauna of early Carnian age) in the basaltic volcaniclastic rocks (Onoue and Tanaka, 2005); and (3)? Ladinian–early Carnian sponge and microproblematica assemblage of reefal limestone blocks that are associated with basaltic rocks (Peybernes et al., 2015). It is widely accepted that the Upper Triassic atoll-type limestone, which overlies oceanic basalts in the Sambosan Belt, was deposited in a low- to middle-latitudinal zone of the western Panthalassa Ocean in a setting having a close paleobiographic affinity with the Tethyan Ocean (Chablais et al., 2011; Stanley and Onoue, 2015). In contrast, foraminiferal assemblages from the limestones in the Taukha Belt are closer to those observed in North American Panthalassan terranes of Oregon and Yukon, suggesting a more eastward origin in the Panthalassa Ocean (Peyrotty et al., 2020).

The contemporaneous emplacement of oceanic and flood basalts in the Sambosan and Taukha belts and Wrangellia may suggest a single LIP origin for all these basalts. This single LIP origin is hypothetical, as there is currently no geochemical or paleolatitude evidence that the basalts of the Sambosan and Taukha belts and the flood basalts of Wrangellia were erupted from the same LIP. However, this hypothesis may be tested in the future, and we have shown the estimated eruption sites of each basalt on the paleogeographic map in Fig. 9. The hypothetical location for this Carnian LIP, which we tentatively term the Wrangellia LIP (Fig. 9), should be tested with new data from accretionary complexes in the circum-Pacific region. For example, Upper Jurassic to Lower Cretaceous accretionary complexes in the Philippines contain numerous Upper Triassic atoll-type limestones (Kiessling and Flügel, 2000) deposited on the top of basaltic seamounts on the Izanagi Plate (Zamoras and Matsuoka, 2004). Paleobiogeographic study of the Upper Triassic benthic foraminifers suggests that these Late Triassic seamounts (Kiessling and Flügel, 2000) were located at low to middle latitudes of the southern hemisphere (Chablais et al., 2010), and may have been western remnants of the Wrangellia LIP (Fig. 9A).

5.3. *Mid-Carnian environmental changes*

Mantle plume activity in an open-ocean setting can cause global environmental changes, as is widely known from mid-Cretaceous strata worldwide (e.g. Erba, 2004; Tejada et al., 2009). The emplacement of the Wrangellia LIP in the Panthalassa Ocean is thought to have caused significant environmental changes in the Carnian (e.g. Furin et al., 2006; Dal Corso et al., 2012; Simms and Ruffell, 2018; Sun et al., 2018).

The negative $\delta^{13}C_{org}$ excursions (NCIE-α and -β) in the Julian 2

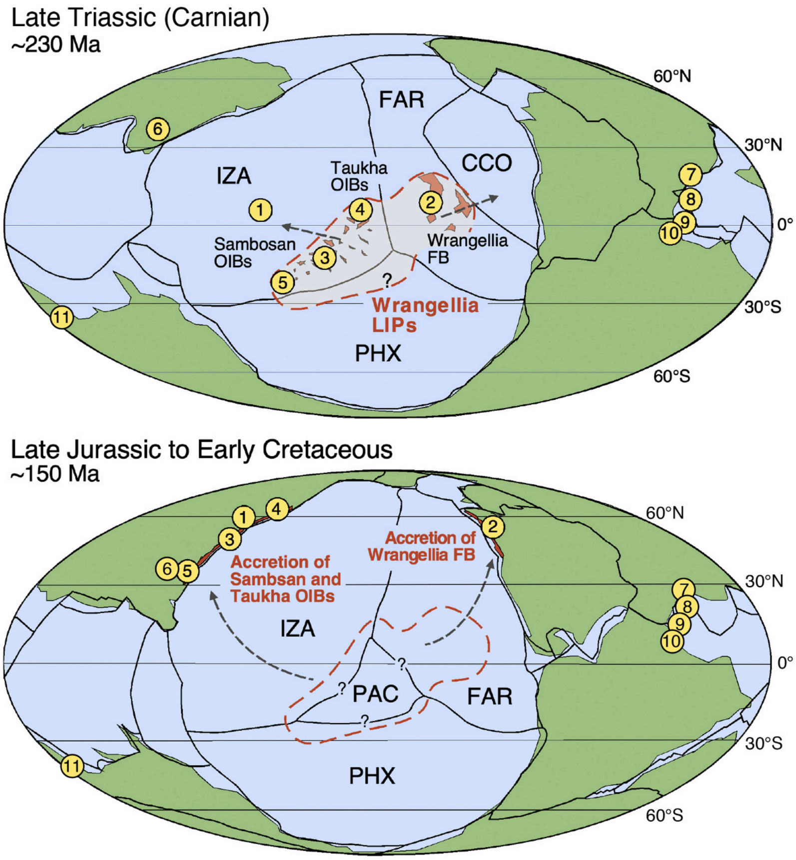

Fig. 9. Maps showing the paleogeography in the Late Triassic and Late Jurassic to Cretaceous and the main marine sections mentioned in the text: 1. Mino Belt, Japan; 2. Wrangellia, British Columbia and Alaska; 3. Sambosan Belt, Japan; 4. Taukha Belt, Far East Russia; 5. North Palawan Block, Philippines; 6. South China Block, China; 7. Northern Calcareous Alps; 8. Dolomites, Southern Alps; 9. Sicily; 10. Tunisia; 11. India Himalaya. The hypothetical location of the Wrangellia Large Igneous Province (LIP) is shown on the Carnian paleogeographic map. The Wrangellia and Sambosan–Taukha basalts were accreted to western North America and East Asia, respectively, in the Late Jurassic to Early Cretaceous. Plate reconstructions and boundaries are redrawn from Müller et al. (2016) and Matthews et al. (2016). Abbreviations: IZA = Izanagi Plate, FAR = Farallon Plate, CCO = Cache Creek Ocean, PHX = Phoenix Plate, and PAC = Pacific Plate.

recorded in Section N—O correspond to the widely recognized negative excursions in marine δ^{13}C records (Fig. 10; Dal Corso et al., 2012, 2015, 2018; Sun et al., 2016). However, marine δ^{13}C records from the northwestern Tethys show different variation patterns in the Julian 2 (Fig. 10; Dal Corso et al., 2012, 2015, 2018). Dal Corso et al. (2018) recognized three NCIEs (NCIE-1 to −3) during the Julian. NCIE-2 was attributed to the input of terrestrial plants (e.g. pollen and spores). Since the bedded cherts in our studied sections are pelagic deep-sea sediments that accumulated far from a continent, the NCIE-2 derived from terrestrial organic carbon would not have been recorded in our studied section. The cause of these globally recognized δ^{13}C excursions during the Julian 2 has been explained by: (1) an injection of ^{13}C-depleted CO_2 into the atmosphere–ocean system during the eruption of the Wrangellia LIP; (2) a combination of volcanic emissions and subsequent methane release (Dal Corso et al., 2012, 2018; Miller et al., 2017; Sun et al., 2018). Both processes could explain the negative $\delta^{13}C_{org}$ excursions in the mid-oceanic realm of the Panthalassa Ocean. Our Os isotope data confirm the initiation of Wrangellia LIP volcanism before NCIE-α. One possible explanation for this discrepancy is that the two NCIEs (NCIE-α and -β) during the Julian 2 imply a more intensive volcanic input of C-depleted CO_2 than during the volcanic pulse of Julian 1, although the ^{12}C enrichment that would have resulted from this scenario was not plausible enough to affect the marine δ^{13}C records in the studied section.

In the present study, redox conditions of seawater overlying the sediments were inferred from the enrichments of V and U. These elements in sediments are useful proxies for moderately to strongly reducing depositional conditions (Sadiq, 1988; Calvert and Pedersen, 1993, 2007; Algeo and Maynard, 2004; Tribovillard et al., 2006). In oxic seawater, V is present as soluble V(V) in the quasi-conservative form of vanadate oxyanions (HVO_4^{2-} and $H_2VO_4^{2-}$). When the redox condition changes from oxic to mildly reducing, V(V) converts to V(IV) and forms the vanadyl ion (VO^{2+}), related hydroxyl species ($VO(OH)_3^-$), and insoluble hydroxides ($VO(OH)_2$) (Breit and Wanty, 1991; Wanty and Goldhaber, 1992). Under such reducing conditions, soluble U(VI) is reduced to insoluble U(IV).

Our data suggest that the studied section records significant redox changes in the pelagic deep-sea Panthalassa in the Julian 2. V_{EF} and U_{EF} abruptly increase in the upper part of the *Ni.*? *budaensis* Zone, which overlaps with the NCIE-β. This result indicates that dysoxic to anoxic conditions were temporarily widespread in the pelagic deep-sea Panthalassa at the end of the Julian 2. Although anoxic conditions in the ocean are commonly associated with positive carbon isotope excursions, we infer that the effects from Wrangellia LIP volcanism dominated the organic carbon isotope record (Dal Corso et al., 2018, 2020), rather than the low-oxygen conditions in the deep-sea. We further examined possible euxinic conditions in the upper part of the *Ni.*? *budaensis* Zone, based on the enrichment of Mo (Calvert and Pedersen, 2007; Takahashi et al., 2014). However, Mo_{EF} is constantly low in the studied section (Supplementary Table S4). Similarly, there is no significant change in the enrichment factors of Ni, Cu, and Zn (Supplementary Tables S3 and S4), which form highly insoluble sulfides and are usually removed from solution in the presence of H_2S (Calvert and Pedersen, 1993, 2007; Algeo and Maynard, 2004). Therefore, we consider the upper part of the *Ni.*? *budaensis* Zone to represent a range of redox conditions from dysoxic to anoxic.

Marine anoxia in the Julian 2 has been recognized from the widespread deposition of black shales and organic-rich marls in several Tethyan basin and along peri-Gondwanan margins (e.g. Sicily, the Northern Calcareous Alps, India, the Dolomites, the Southern Alps, Tunisia, and South China; Bellanca et al., 1995; Keim et al., 2006; Hornung et al., 2007a, 2007b; Soua, 2014; Sun et al., 2016) (Fig. 9). Our geochemical data provide the first evidence of the low oxygen (dysoxic to anoxic) conditions in the pelagic deep-sea Panthalassa Ocean, which indicates that Julian 2 marine anoxia may have developed from the

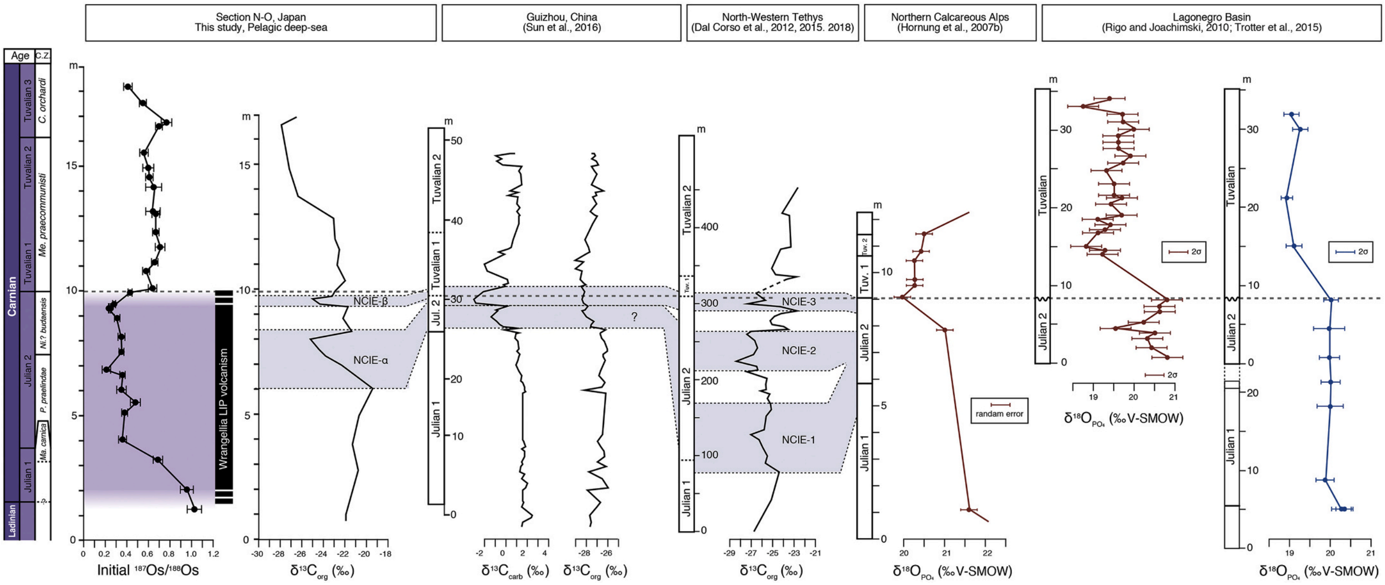

Fig. 10. Organic carbon isotope records from the pelagic deep-sea Panthalassa (this study), South China (Sun et al., 2016), and NW Tethys (Dal Corso et al., 2012, 2015, 2018), compared with initial ^{187}Os/^{188}Os ratios from the study section. Paleotemperatures calculated from oxygen isotope compositions of conodont apatite ($\delta^{18}O_{PO4}$) from Northern Calcareous Alps (NCA; Hornung et al., 2007b) and Lagonegro Basin (LA; Rigo and Joachimski, 2010; Trotter et al., 2015) are also shown for comparison. Red and blue of lines indicate the data for oxygen-isotope compositions of conodont apatite determined by gas isotope ratio mass spectrometry (GIRMS) and sensitive high-resolution ion microprobe (SHRIMP), respectively. (For interpretation of the references to colour in this figure legend, the reader is referred to the web version of this article.)

shallow continental margin to the deep-sea Panthalassa Ocean. One possible cause of the anoxia is increased global continental weathering during the CPE (Hornung et al., 2007b; Rigo et al., 2007). However, seawater $^{187}Os/^{188}Os_i$ ratios increased abruptly after a period of low-oxygen seawater conditions, which may have been due to a sudden increase in radiogenic Os inputs from continental weathering induced by higher mean temperatures of Earth's surface. Such increased temperatures in the Julian 2 are supported by a decrease in conodont apatite oxygen isotopic compositions across the Julian–Tuvalian boundary from the western Tethys (Fig. 10; Hornung et al., 2007b; Rigo and Joachimski, 2010; Trotter et al., 2015). Therefore, these studies demonstrate no apparent link between increased chemical weathering and the development of anoxic conditions during the Julian 2. Further geochemical research, such as oxygen isotope compositions of conodont apatite and sulfur isotopes will help to constrain the cause of the onset and development of anoxic conditions during the Julian 2.

6. Conclusions

In order to clarify the temporal relationship between the eruption of the Wrangellia LIP and CPE, we undertook a high-resolution paleo-seawater Os isotope and conodont–radiolarian biostratigraphic study of an Upper Triassic bedded chert succession in the Inuyama area, Japan. Redox-sensitive element concentrations and a carbon isotope profile were also obtained to understand the environmental changes during the CPE. Our main conclusions are as follows.

1. We established conodont biozones based on the FOs of the representative conodont species of each zone in the upper Ladinian to upper Carnian (Tuvalian) interval in Section N—O. In chronological order, these are the *Ma. carnica*, *P. praelindae, Ni.*? *budaensis*, *Me. praecommunisti*, and *C. orchardi* zones. These conodont zones are comparable to the standard Carnian conodont zones of the Tethys.
2. Two negative $\delta^{13}C_{org}$ excursions (NCIE-α and -β) during the Julian 2 correlate with the globally recognized negative excursions in marine $\delta^{13}C_{org}$ records from Europe and South China.
3. High-resolution Os isotope data and our biostratigraphic analysis revealed: (i) a continuous decrease in $^{187}Os/^{188}Os_i$ ratios in the Julian 1; (ii) low and steady $^{187}Os/^{188}Os_i$ ratios in the Julian 2; (iii) an abrupt $^{187}Os/^{188}Os_i$ ratio increase at the end of the Julian 2. The unradiogenic $^{187}Os/^{188}Os_i$ values in the Julian are attributable to a mantle-derived influx of unradiogenic Os associated with the Wrangellia LIP.
4. High abundances of V and U in the late Julian 2 indicate that the pelagic deep-sea Panthalassa Ocean was temporarily in low oxygen (dysoxic to anoxic) conditions, which overlaps with NCIE-β. Such anoxic conditions during the Julian 2 have been documented from the deposition of black shales and organic-rich marls in intermediate to shallow-water Tethyan sections. These studies suggest the ocean anoxia may have existed from the shallow continental margin to the deep-sea Panthalassa Ocean in the Julian 2.

Declaration of Competing Interest

The authors declare that they have no known competing financial interests or personal relationships that could have appeared to influence the work reported in this paper.

Acknowledgements

We thank Y. Otsuki and H. Yamamoto of JAMSTEC for their assistance with the Re—Os isotope and ICP-MS analyses. This study was supported by the Japan Society for the Promotion of Science (Grant JP17J11607 to Y. Tomimatsu; Grants JP17H02975 and JP15H05771 to T. Onoue). We also thank Svetoslav Georgiev and an anonymous reviewer for helpful and thoughtful reviews.

Appendix A. Supplementary data

Supplementary data to this article can be found online at https://doi.org/10.1016/j.gloplacha.2020.103387.

References

Algeo, T.J., Maynard, B.J., 2004. Trace-element behavior and redox facies in core shales of Upper Pennsylvanian Kansas-type cyclothems. Chem. Geol. 206, 289–318. https://doi.org/10.1016/j.chemgeo.2003.12.009.

Allègre, C.J., Louvat, P., Gaillardet, J., Meynadier, L., Rad, S., Capmas, F., 2010. The fundamental role of island arc weathering in the oceanic Sr isotope budget. Earth Planet. Sci. Lett. 292, 51–56. https://doi.org/10.1016/j.epsl.2010.01.019.

Ando, A., Kodama, K., Kojima, S., 2001. Low-latitude and southern hemisphere origin of Anisian (Triassic) bedded chert in the Inuyama area, Mino terrane, Central Japan. J. Geophys. Res. 106, 1973–1986. https://doi.org/10.1029/2000JB900305.

Balini, M., Lucas, S.G., Jenks, J.F., Spielmann, J.A., 2010. Triassic ammonoid biostratigraphy: an overview. Geol. Soc. Lond., Spec. Publ. 334, 221–262. https://doi.org/10.1144/SP334.10.

Balini, M., Krystyn, L., Levera, M., Tripodo, A., 2012. Late Carnian-Early Norian ammonoids from the GSSP candidate section Pizzo Mondello (Sicani Mountains, Sicily). Riv. Ital. Paleontol. S 118, 47–84. https://doi.org/10.13130/2039-4942/5992.

Baranyi, V., Rostási, Á., Raucsik, B., Kürschner, W.M., 2019. Palynology and weathering proxies reveal climatic fluctuations during the Carnian Pluvial Episode (CPE) (late Triassic) from marine successions in the Transdanubian Range (western Hungary). Glob. Planet. Chang. 177, 157–172. https://doi.org/10.1016/j.gloplacha.2019.01.

Bellanca, A., Di Stefano, P., Neri, R., 1995. Sedimentology and isotope geochemistry of Carnian deep-water marl/limestone deposits from the Sicani Mountains, Sicily: environmental implications and evidence for a planktonic source of lime mud. Palaeogeogr. Palaeoclimatol. Palaeoecol. 114, 111–129. https://doi.org/10.1016/0031-0182(95)00077-Y.

Benton, M.J., 1986. More than one event in the Late Triassic mass extinction. Nature 321, 857–861. https://doi.org/10.1038/321857a0.

Benton, M.J., Bernardi, M., Kinsella, C., 2018. The Carnian Pluvial Episode and the origin of dinosaurs. J. Geol. Soc. Lond. 175, 1019–1026. https://doi.org/10.1144/jgs2018-049.

Bernardi, M., Gianolla, P., Petti, F.M., Mietto, P., Benton, M.J., 2018. Dinosaur diversification linked to the Carnian Pluvial Episode. Nat. Commun. 9, 1499. https://doi.org/10.1038/s41467-018-03996-1.

Breit, G.N., Wanty, R.B., 1991. Vanadium accumulation in carbonaceous rocks: a review of geochemical controls during deposition and diagenesis. Chem. Geol. 91, 83–97. https://doi.org/10.1016/0009-2541(91)90083-4.

Callegaro, S., Rigo, M., Chiaradia, M., Marzoli, A., 2012. Latest Triassic marine Sr isotopic variations, possible causes and implications. Terra Nova 24, 130–135. https://doi.org/10.1111/j.1365-3121.2011.01046.x.

Calvert, S.E., Pedersen, T.F., 1993. Geochemistry of recent oxic and anoxic marine sediments: implications for the geological record. Mar. Geol. 113, 67–88. https://doi.org/10.1016/0025-3227(93)90150-T.

Calvert, S.E., Pedersen, T.F., 2007. Elemental proxies for palaeoclimatic and palaeoceanographic variability in marine sediments: Interpretation and application. In: Hillaire-Marcel, C., De Vernal, A. (Eds.), Proxies in Late Cenozoic Paleoceanography. Dev. Mar. Geol, vol. 1, pp. 567–644. https://doi.org/10.1016/S1572-5480(07)01019-6.

Carlisle, D., Susuki, T., 1974. Emergent basalt and submergent carbonate-clastic sequences including Upper Triassic Dilleri and Welleri zones on Vancouver Island. Can. J. Earth Sci. 11, 254–279. https://doi.org/10.1139/e74-023.

Chablais, J., Onoue, T., Martini, R., 2010. Upper Triassic reef-limestone blocks of southwestern Japan: new data from a Panthalassan seamount. Palaeogeogr. Palaeoclimatol. Palaeoecol. 293, 206–222. https://doi.org/10.1016/j.palaeo.2010.05.022.

Chablais, J., Martini, R., Kobayashi, F., Stampfli, G.M., Onoue, T., 2011. Upper Triassic foraminifers from Panthalassan carbonate buildups of southwestern Japan and their paleobiogeographic implications. Micropaleontology 57, 93–124.

Cohen, A.S., Coe, A.L., 2002. New geochemical evidence for the onset of volcanism in the Central Atlantic magmatic province and environmental change at the Triassic-Jurassic boundary. Geology 30, 267–270. https://doi.org/10.1130/0091-7613(2002)030<0267:NGEFTO>2.0.CO;2.

Dal Corso, J., Mietto, P., Newton, R.J., Pancost, R.D., Preto, N., Roghi, G., Wignall, P.B., 2012. Discovery of a major negative $\delta^{13}C$ spike in the Carnian (Late Triassic) linked to the eruption of Wrangellia flood basalts. Geology 40, 79–82. https://doi.org/10.1130/g32473.1.

Dal Corso, J., Gianolla, P., Newton, R.J., Franceschi, M., Roghi, G., Caggiati, M., Raucsik, B., Budai, T., Haas, J., Preto, N., 2015. Carbon isotope records reveal synchronicity between carbon cycle perturbation and the "Carnian Pluvial Event" in the Tethys realm (Late Triassic). Glob. Planet. Chang. 127, 79–90. https://doi.org/10.1016/j.gloplacha.2015.01.013.

Dal Corso, J., Gianolla, P., Rigo, M., Franceschi, M., Roghi, G., Mietto, P., Manfrin, S., Raucsik, B., Budai, T., Jenkyns, H.C., Reymond, C.E., Caggiati, M., Gattolin, G., Breda, A., Merico, A., Preto, N., 2018. Multiple negative carbon-isotope excursions during the Carnian Pluvial Episode (late Triassic). Earth-Sci. Rev. 185, 732–750. https://doi.org/10.1016/j.earscirev.2018.07.004.

Dal Corso, J., Bernardi, M., Sun, Y.D., Song, H., Seyfullah, L.J., Preto, N., Gianolla, P., Ruffell, A., Kustatscher, E., Roghi, G., Merico, A., Hohn, S., Schmidt, A.R., Marzoli, A., Newton, R.J., Wignall, P.B., Benton, M.J., 2020. Extinction and dawn of the modern world in the Carnian (Late Triassic). Sci. Adv. 6 https://doi.org/10.1126/sciadv.aba0099 eaba0099.

Erba, E., 2004. Calcareous nannofossils and Mesozoic oceanic anoxic events. Mar. Micropaleontol. 52, 85–106. https://doi.org/10.1016/j.marmicro.2004.04.007.

Erba, E., 2006. The first 150 million years history of calcareous nannoplankton: biosphere–geosphere interactions. Palaeogeogr. Palaeoclimatol. Palaeoecol. 232, 237–250. https://doi.org/10.1016/j.palaeo.2005.09.013.

Faure, M., Natal'in, B., 1992. The geodynamic evolution of the eastern Eurasian margin in Mesozoic times. Tectonophysics 208, 397–411. https://doi.org/10.1016/0040-1951(92)90437-B.

Furin, S., Preto, N., Rigo, M., Roghi, G., Gianolla, P., Crowley, J.L., Bowring, S.A., 2006. High-precision U–Pb zircon age from the Triassic of Italy: implications for the Triassic time scale and the Carnian origin of calcareous nannoplankton and dinosaurs. Geology 34, 1009–1012. https://doi.org/10.1130/G22967A.

Gao, P., Santosh, M., Nakagawa, M., Li, S.S., 2018. Ocean island basalts and sedimentary units in the accretionary complex of Kochi, SW Japan: implications for convergent margin tectonics and arc subduction. Geol. J. 55, 533–552. https://doi.org/10.1002/gj.3436.

Georgiev, S., Stein, H.J., Hannah, J.L., Weiss, H.M., Bingen, B., Xu, G., Rein, E., Hatlø, V., Løseth, H., Nali, M., Piasecki, S., 2012. Chemical signals for oxidative weathering predict Re–Os isochroneity in black shales, East Greenland. Chem. Geol. 324-325, 108–121. https://doi.org/10.1016/j.chemgeo.2012.01.003.

Greene, A.R., Scoates, J.S., Weis, D., Katvala, E.C., Israel, S., Nixon, G.T., 2010. The architecture of oceanic plateaus revealed by the volcanic stratigraphy of the accreted Wrangellia oceanic plateau. Geosphere 6, 47–73. https://doi.org/10.1130/GES00212.1.

Hampton, B.A., Ridgway, K.D., Gehrels, G.E., 2010. A detrital record of Mesozoic island arc accretion and exhumation in the north American Cordillera: U-Pb geochronology of the Kahiltna basin, southern Alaska. Tectonics 29, TC4015. https://doi.org/10.1029/2009TC002544.

Hassler, D.R., Peucker-Ehrenbrink, B., Ravizza, G.E., 2000. Rapid determination of Os isotopic composition by sparging OsO_4 into a magnetic-sector ICP-MS. Chem. Geol. 166, 1–14. https://doi.org/10.1016/S0009-2541(99)00180-1.

Hillhouse, J.W., Gromme, C.S., 1984. Northward displacement and accretion of Wrangellia: new paleomagnetic evidence from Alaska. J. Geophys. Res. 89, 4461–4477. https://doi.org/10.1029/JB089iB06p04461.

Hori, R.S., Cho, C.F., Umeda, H., 1993. Origin of cyclicity in Triassic-Jurassic radiolarian bedded cherts of the Mino accretionary complex from Japan. Island Arc 3, 170–180. https://doi.org/10.1111/j.1440-1738.1993.tb00084.x.

Hornung, T., Krystyn, L., Brandner, R., 2007a. A Tethys-wide mid-Carnian (Upper Triassic) carbonate productivity decline: evidence for the Alpine Reingraben Event from Spiti (Indian Himalaya)? J. Asian Earth Sci. 30, 285–302. https://doi.org/10.1016/j.jseaes.2006.10.001.

Hornung, T., Brandner, R., Krystyn, L., Joachimski, M.M., Keim, L., 2007b. Multistratigraphic constraints on the NW Tethyan "Carnian Crisis". N. M. Mus. Nat. Hist. Sci. Bull. 4, 9–67.

Ikeda, M., Tada, R., 2014. A 70 million year astronomical time scale for the deep-sea bedded chert sequence (Inuyama, Japan): implications for Triassic–Jurassic geochronology. Earth Planet. Sci. Lett. 399, 30–43. https://doi.org/10.1016/j.epsl.2014.04.031.

Ikeda, M., Tada, R., Sakuma, H., 2010. Astronomical cycle origin of bedded chert: a middle Triassic bedded chert sequence, Inuyama, Japan. Earth Planet. Sci. Lett. 297, 369–378. https://doi.org/10.1016/j.epsl.2010.06.027.

Ikeda, M., Tada, R., Ozaki, K., 2017. Astronomical pacing of the global silica cycle recorded in Mesozoic bedded cherts. Nat. Commun. 8, 15532. https://doi.org/10.1038/ncomms15532.

Ishida, K., Hirsch, F., 2001. Taxonomy and faunal affinity of Late Carnian–Rhaetian conodonts in the Southern Chichibu Belt, Shikoku, SW Japan. Riv. Ital. Paleontol. S 107, 227–250. https://doi.org/10.13130/2039-4942/5433.

Ishizuka, O., Taylor, R.N., Milton, J.A., Nesbitt, R.W., 2003. Fluid–mantle interaction in an intra-oceanic arc: constraints from high-precision Pb isotopes. Earth Planet. Sci. Lett. 211, 221–236. https://doi.org/10.1016/S0012-821X(03)00201-2.

Isozaki, Y., 1996. Anatomy and genesis of a subduction-related orogen: a new view of geotectonic subdivision and evolution of the Japanese Islands. Island Arc 5, 289–320. https://doi.org/10.1111/j.1440-1738.1996.tb00033.x.

Jiang, H., Tuan, J., Chen, Y., Ogg, J.G., Yan, J., 2019. Synchronous onset of the Mid-Carnian Pluvial Episode in the East and West Tethys: conodont evidence from Hanwang, Sichuan, South China. Palaeogeogr. Palaeoclimatol. Palaeoecol. 520, 173–180. https://doi.org/10.1016/j.palaeo.2019.02.004.

Jin, X., Gianolla, P., Shi, Z., Franceschi, M., Caggiati, M., Du, Y., Preto, N., 2020. Synchronized changes in shallow water carbonate production during the Carnian Pluvial Episode (Late Triassic) throughout Tethys. Glob. Planet. Chang. 184, 103035. https://doi.org/10.1016/j.gloplacha.2019.103035.

Jones, D.L., Silberling, N.J., Hillhouse, J., 1977. Wrangellia - a displaced terrane in northwestern North America. Can. J. Earth Sci. 14, 2565–2577. https://doi.org/10.1139/e77-222.

Keim, L., Spötl, C., Brandner, R., 2006. The aftermath of the Carnian carbonate platform demise: a basinal perspective (Dolomites, Southern Alps). Sedimentology 53, 361–386. https://doi.org/10.1111/j.1365-3091.2006.00768.x.

Kent, D.V., Olsen, P.E., Muttoni, G., 2017. Astrochronostratigraphic polarity time scale (APTS) for the late Triassic and Early Jurassic from continental sediments and correlation with standard marine stages. Earth-Sci. Rev. 166, 153–180. https://doi.org/10.1016/j.earscirev.2016.12.014.

Khanchuk, A.I., Nikitina, A.P., Panchenko, I.V., Buriy, G.I., Kemkin, I.V., 1989. Paleozoic and Mesozoic guyots of the Sikhote-Alin and Sakhalin. Dokl. Acad. Sci. SSSR 307, 186–190 (in Russian).

Kiessling, W., Flügel, E., 2000. Late paleozoic and Late Triassic limestones from North Palawan Block (Philippines): microfacies and paleogeographical implications. Facies 43, 39–77. https://doi.org/10.1007/BF02536984.

Kimura, K., Hori, R., 1993. Offscraping accretion of Jurassic chert-clastic complexes in the Mino–Tamba belt, Central Japan. J. Struct. Geol. 15, 145–161. https://doi.org/10.1016/0191-8141(93)90092-O.

Kimura, J.-I., Nozaki, T., Senda, R., Suzuki, K., 2014. Precise determination of Os isotope ratios in the 15-4000 pg range using a sparging method using enhanced-sensitivity multiple Faraday collector- inductively coupled plasma-mass spectrometry. J. Anal. Atom. Spectrom. 29, 1483–1490. https://doi.org/10.1039/c4ja00092g.

Kojima, S., 1989. Mesozoic terrane accretion in Northeast China, Sikhote-Alin and Japan regions. Palaeogeogr. Palaeoclimatol. Palaeoecol. 69, 213–232. https://doi.org/10.1016/0031-0182(89)90165-X.

Kojima, S., Kemukin, I.V., Kametaka, M., Ando, A., 2000. A correlation of accretionary complexes of southern Sikhote-Alin of Russia and Inner Zone of Southwest Japan. Geosci. J. 4, 175–185. https://doi.org/10.1007/BF02910136.

Kolar-Jurkovšek, T., Jurkovšek, B., 2010. New paleontological evidence of the Carnian strata in the Mežica area (Karavanke Mountains, Slovenia): conodont data for the Carnian Pluvial Event. Palaeogeogr. Palaeoclimatol. Palaeoecol. 290, 81–88. https://doi.org/10.1016/j.palaeo.2009.06.015.

Kolar-Jurkovšek, T., Gaździcki, A., Jurkovšek, B., 2005. Conodonts and foraminifera from the "Raibl Beds" (Carnian) of the Kararvanke Mountains, Slovenia: stratigraphical and paleontological implications. Geol. Q 4, 429–438.

Korte, C., Kozur, H.W., Bruckschen, P., Veizer, J., 2003. Strontium isotope evolution of Late Permian and Triassic seawater. Geochim. Cosmochim. Acta 67, 47–62. https://doi.org/10.1016/S0016-7037(02)01035-9.

Kozur, H., Mock, R., 1991. New Middle Carnian and Rhaetian conodonts from Hungary and the Alps, stratigraphic importance and tectonic implications for the Buda Mountains and adjacent areas. Jahrb. Geol. Bundesanst. 134, 271–297.

Kozur, H., Mostler, H., 1994. Anisian to Middle Carnian radiolarian zonation and description of some stratigraphically important radiolarians. Geol. Paläont. Mitt. Innsbr. Sonderbd. 3, 39–255.

Kozur, H., Krainer, K., Mostler, H., 1994. Middle Triassic conodonts from the southern Karawanken Mountains (Southern Alps) and their stratigraphic importance. Geol. Paläont. Mitt. Innsbr. Bd. 19, 165–200.

Kuroda, J., Hori, R.S., Suzuki, K., Gröcke, D.R., Ohkouchi, N., 2010. Marine osmium isotope record across the Triassic-Jurassic boundary from a Pacific pelagic site. Geology 38, 1095–1098. https://doi.org/10.1130/G31223.1.

Levasseur, S., Birck, J.L., Allègre, C.J., 1999. The osmium riverine flux and the oceanic mass balance of osmium. Earth Planet. Sci. Lett. 174, 7–23. https://doi.org/10.1016/S0012-821X(99)00259-9.

López-Gómez, J., Escudero-Mozo, M.J., Martín-Chivelet, J., Arche, A., Lago, M., Galé, C., 2017. Western Tethys continental-marine responses to the Carnian Humid Episode: palaeoclimatic and palaeogeographic implications. Glob. Planet. Chang. 148, 79–95. https://doi.org/10.1016/j.gloplacha.2016.11.016.

Lucas, S.G., 2018. Late Triassic ammonoids: Distribution, biostratigraphy and biotic events. In: Tanner, L. (Ed.), The Late Triassic World. Topics in Geobiology, 46. Springer Publ, pp. 237–262. https://doi.org/10.1007/978-3-319-68009-5_7.

Lucas, S.G., Tanner, L.H., 2018. The missing mass extinction at the Triassic-Jurassic boundary. In: Tanner, L. (Ed.), The Late Triassic World. Topics in Geobiology, 46. Springer Publ, pp. 721–785. https://doi.org/10.1007/978-3-319-68009-5_15.

Maron, M., Muttoni, G., Rigo, M., Gianolla, P., Kent, D.V., 2019. New magnetobiostratigraphic results from the Ladinian of the Dolomites and implications for the Triassic geomagnetic polarity timescale. Palaeogeogr. Palaeoclimatol. Palaeoecol. 517, 52–73. https://doi.org/10.1016/j.palaeo.2018.11.024.

Matsuda, T., Isozaki, Y., 1991. Well-documented travel history of Mesozoic pelagic chert in Japan: from remote ocean to subduction zone. Tectonics 10, 475–499. https://doi.org/10.1029/90TC02134.

Matsuoka, A., 1992. Jurassic-early cretaceous tectonic evolution of the Southern Chichibu terrane, Southwest Japan. Palaeogeogr. Palaeoclimatol. Palaeoecol. 96, 71–88. https://doi.org/10.1016/0031-0182(92)90060-I.

Matsuoka, A., Hori, R., Kuwahara, K., Hiraishi, M., Yao, A., Ezaki, Y., 1994. Triassic-Jurassic radiolarian-bearing sequences in the Mino terrane, Central Japan. Guide Book of InterRad VII Field Excursion 19–61.

Matthews, K.J., Maloney, K.T., Zahirovic, S., Williams, S.E., Seton, M., Müller, R.D., 2016. Global plte boundary evolution and Kinematics since the late Paleozoic. Glob. Planet. Chang. 146, 226–250. https://doi.org/10.1016/j.gloplacha.2016.10.002.

Mazza, M., Rigo, M., Nicora, A., 2011. A new *Metapolygnathus* platform conodont species and its implications for Upper Carnian global correlations. Acta Palaeontol. Pol. 56, 121–131. https://doi.org/10.4202/app.2009.1104.

Mazza, M., Rigo, M., Gullo, M., 2012. Taxonomy and biostratigraphic record of the Upper Triassic conodonts of the Pizzo Mondello section (Western Sicily, Italy), GSSP candidate for the base of the Norian. Riv. Ital. Paleontol. S 118, 85–130. https://doi.org/10.13130/2039-4942/5993.

Mietto, P., Manfrin, S., Preto, N., Rigo, M., Roghi, G., Furin, S., Gianolla, P., Posenato, R., Muttoni, G., Nicora, A., Buratti, N., Cirilli, S., Spötl, C., Ramezani, J., Bowring, S.A., 2012. The global boundary stratotype section and Point (GSSP) of the Carnian Stage (Late Triassic) at Prati di Stuores/Stuores Wiesen section (Southern Alps, NE Italy). Episodes 35, 414–430. https://doi.org/10.18814/epiiugs/2012/v35i3/003.

Miller, C.S., Peterse, F., da Silva, A.C., Baranyi, V., Reichart, G.J., Kürschner, W.M., 2017. Astronomical age constraints and extinction mechanisms of the late Triassic Carnian crisis. Sci. Rep. 7, 2557. https://doi.org/10.1038/s41598-017-02817-7.

Morgan, J.W., Golightly, D.W., Dorrzapf, A.F., 1991. Methods for the separation of rhenium, osmium and molybdenum applicable to isotope geochemistry. Talanta 38, 259–265. https://doi.org/10.1016/0039-9140(91)80045-2.

Mortensen, J.K., Hulbert, L.J., 1992. A U-Pb zircon age for a Maple Creek gabbro sill, Tatamagouche Creek area, southwest Yukon Territory, Radiogenic age and isotopic studies: Report 5. In: Geol. Surv. Can. Paper, pp. 175–179. https://doi.org/10.4095/132923.

Mueller, S., Krystn, L., Kürschner, W.M., 2016. Climate variability during the Carnian Pluvial Phase - A quantitative palynological study of the Carnian sedimentary succession at Lunz am See, Northern Calcareous Alps, Austria. Palaeogeogr. Palaeoclimatol. Palaeoecol. 441, 198–211. https://doi.org/10.1016/j.palaeo.2015.06.008.

Müller, R.D., Seton, M., Zahirovic, S., Williams, S.E., Matthews, K.J., Wright, N.M., Shephard, G.E., Maloney, K.T., Barnett-Moore, N., Hosseinpour, M., Bower, D.J., Cannon, J., 2016. Ocean basin evolution and global-scale plate reorganization events since Pangea breakup. Annu. Rev. Earth Planet. Sci. 44, 107–138. https://doi.org/10.1146/annurev-earth-060115-012211.

Mundil, R., Pálfy, J., Renne, P.R., Brack, P., 2010. The Triassic timescale: New constraints and a review of geochronological data. In: Lucas, S.G. (Ed.), The Triassic Timescale, 334. Geol. Soc. Lond., Spec. Publ, pp. 41–60. https://doi.org/10.1144/SP334.3.

Nakada, R., Ogawa, K., Suzuki, N., Takahashi, S., Takahashi, Y., 2014. Late Triassic compositional changes of aeolian dusts in the pelagic Panthalassa: response to the continental climatic change. Palaeogeogr. Palaeoclimatol. Palaeoecol. 393, 61–75. https://doi.org/10.1016/j.palaeo.2013.10.014.

Nozaki, T., Suzuki, K., Ravizza, G., Kimura, J.-I., Chang, Q., 2012. A method for rapid determination of Re and Os isotope compositions using ID-MC-ICP-MS combined with the sparging method. Geostand. Geoanal. Res. 36, 131–148. https://doi.org/10.1111/j.1751-908X.2011.00125.x.

Nozaki, T., Nikaido, T., Onoue, T., Takaya, Y., Sato, K., Kimura, J.-I., Chang, Q., Yamashita, D., Sato, H., Suzuki, K., Kato, Y., Matsuoka, A., 2019. Triassic marine Os isotope record from a pelagic chert succession, Sakahogi section, Mino Belt, Southwest Japan. J. Asian Earth Sci. X 1, 100004. https://doi.org/10.1016/j.jaesx.2018.100004.

Ogg, J.G., 2012. Triassic. In: Gradstein, F.M., Ogg, J.G., Schmitz, M., Ogg, G. (Eds.), The Geologic Time Scale 2012. Elsevier Publ, pp. 681–730. https://doi.org/10.1016/B978-0-444-59425-9.00025-1.

Ogg, J.G., 2015. The mysterious Mid-Carnian "Wet Intermezzo" global event. J. Earth Sci. 26, 181–191. https://doi.org/10.1007/s12583-015-0527-x.

Ogg, J.G., Huang, C., Hinnov, L., 2014. Triassic timescale status: a brief overview. Albertiana 41, 3–30.

Onoue, T., Sano, H., 2007. Triassic mid-oceanic sedimentation in Panthalassa Ocean: sambosan accretionary complex. Japan. Isl. Arc 16, 173–190. https://doi.org/10.1111/j.1440-1738.2007.00565.x.

Onoue, T., Tanaka, H., 2005. Late Triassic bivalves from the Sambosan accretionary complex, Southwest Japan, and their biogeographic implications. Paleontol. Res. 9, 15–25. https://doi.org/10.2517/prpsj.9.15.

Onoue, T., Nagai, K., Kamishima, A., Seno, M., Sano, H., 2004. Origin of basalts from Sambosan accretionary complex, Shikoku and Kyushu. J. Geol. Soc. Japan 110, 222–236 (in Japanese). https://doi.org/10.5575/geosoc.110.222.

Onoue, T., Sato, H., Nakamura, T., Noguchi, T., Hidaka, Y., Shirai, N., Ebihara, M., Osawa, T., Hatsukawa, Y., Toh, Y., Koizumi, M., Harada, H., Orchard, M.J., Nedachi, M., 2012. Deep-sea record of impact approximately unrelated to mass extinction in the late Triassic. Proc. Natl. Acad. Sci. U. S. A. 109, 19134–19139. https://doi.org/10.1073/pnas.1209486109.

Orchard, M.J., 2007. New conodonts and zonation, Ladinian-Carnian boundary beds, British Columbia, Canada. In: Lucas, S.G., Spielman, J.A. (Eds.), The Global Triassic. New Mex. Mus. Nat. Hist. Sci. Bull, vol. 41, pp. 321–330.

Orchard, M.J., 2010. Triassic conodonts and their role in stage boundary definition. In: Lucas, S.G. (Ed.), The Triassic Timescale, 334. Geol. Soc. Lond., Spec. Publ, pp. 139–161. https://doi.org/10.1144/SP334.7.

Orchard, M.J., 2019. The Carnian–Norian boundary GSSP candidate at Black Bear Ridge, British Columbia, Canada: update, correlation, and conodont taxonomy. Albertiana 45, 50–68.

Paquay, F.S., Ravizza, G.E., Dalai, T.K., Reucker-Ehrenbtink, B., 2008. Determining chondritic impactor size from the marine osmium isotope record. Science 320, 214–218. https://doi.org/10.1126/science.1152860.

Parrish, R.R., McNicoll, V.J., 1992. U-Pb determinations from the southern Vancouver Island area, British Columbia, Radiogenic and isotopic studies: Report 5. In: Geol. Surv. Can. Paper, pp. 79–86. https://doi.org/10.4095/132923.

Peucker-Ehrenbrink, B., Jahn, B.-M., 2001. Rhenium-osmium isotope systematics and platinum group element concentrations: loess and the upper continental crust. Geochem. Geophys. Geosyst. 2, 1061. https://doi.org/10.1029/2001GC000172.

Peucker-Ehrenbrink, B., Ravizza, G., 2000. The marine osmium isotope record. Terra Nova 12, 205–219. https://doi.org/10.1046/j.1365-3121.2000.00295.x.

Peucker-Ehrenbrink, B., Ravizza, G., 2012. Os isotope stratigraphy. In: Gradstein, F.M., Ogg, J.G., Schmitz, M., Ogg, G. (Eds.), The Geologic Time Scale 2012. Elsevier Publ, pp. 145–166. https://doi.org/10.1016/B978-0-444-59425-9.00008-1.

Peybernes, C., Chablais, J., Martini, R., 2015. Upper Triassic (Ladinian?-Carnian) reef biota from the Sambosan Accretionary complex, Shikoku, Japan. Facies 61. https://doi.org/10.1007/s10347-015-0446-4.

Peyrotty, G., Rigaud, S., Kemkin, I., Martini, R., 2020. Sedimentology and biostratigraphy of upper Triassic atoll-type carbonates from the Dalnegorsk area, Taukha terrane, far East Russia. Glob. Planet. Chang. 184, 103072. https://doi.org/10.1016/j.gloplacha.2019.103072.

Preto, N., Willems, H., Guaiumi, C., Westphal, H., 2013. Onset of significant pelagic carbonate accumulation after the Carnian Pluvial Event (CPE) in the western Tethys. Facies 59, 891–914. https://doi.org/10.1007/s10347-013-0387-8.

Punina, T.A., 1997. Classification and correlation of Triassic limestones in Sikhote-Alin on the basis of corals. In: Dickins, J.M., Zunyi, Y., Hongfu, Y., Lucas, S.G., Acharyya, S.K. (Eds.), Late Palaeozoic and Early Mesozoic Circum-Pacific Events and their Global Correlation. World and Regional Geology 10. Cambridge Univ. Press, pp. 186–192. https://doi.org/10.1017/CBO9780511564413.021.

Ravizza, G., Peucker-Ehrenbrink, B., 2003. Chemostratigraphic evidence of Deccan volcanism from the marine osmium isotope record. Science 302, 1392–1395. https://doi.org/10.1126/science.1089209.

Rigo, M., Joachimski, M.M., 2010. Palaeoecology of Late Triassic conodonts: constraints from oxygen isotopes in biogenic apatite. Acta Palaeontol. Pol. 55, 471–478. https://doi.org/10.4202/app.2009.0100.

Rigo, M., Preto, N., Roghi, G., Tateo, F., Mietto, P., 2007. A rise in the Carbonate Compensation Depth of western Tethys in the Carnian: deep-water evidence for the Carnian Pluvial Event. Palaeogeogr. Palaeoclimatol. Palaeoecol. 246, 188–205. https://doi.org/10.1016/j.palaeo.2006.09.013.

Rigo, M., Preto, N., Franceschi, M., Guaiumi, C., 2012. Stratigraphy of the Carnian-Norian Calcari con Selce Formation in the Lagonegro Basin, Southern Apennines. Riv. Ital. Paleontol. S 118, 143–154. https://doi.org/10.13130/2039-4942/5995.

Rigo, M., Mazza, M., Karádi, V., Nicora, A., 2018. New Upper Triassic conodont biozonation of the Tethyan Realm. In: Tanner, L. (Ed.), The Late Triassic World. Topics in Geobiology. 46. Springer Publ, pp. 189–235. https://doi.org/10.1007/978-3-319-68009-5_6.

Robinson, N., Ravizza, G., Coccioni, R., Peucker-Ehrenbrink, B., Norris, R.D., 2009. A high-resolution marine ^{187}Os/^{188}Os record for the late Maastrichtian: Distinguishing the chemical fingerprints of Deccan volcanism and the KP impact event. Earth Planet. Sci. Lett. 281, 159–168. https://doi.org/10.1016/j.epsl.2009.02.019.

Roghi, G., Gianolla, P., Minarelli, L., Pilati, C., Preto, N., 2010. Palynological correlation of Carnian humid pulses throughout western Tethys. Palaeogeogr. Palaeoclimatol. Palaeoecol. 290, 89–106. https://doi.org/10.1016/j.palaeo.2009.11.006.

Rudnick, R.L., Gao, S., 2014. Composition of the Continental Crust. In: Holland, H.D., Turekian, K.K. (Eds.), Treatise on Geochemistry, vol. 4. Elsevier Sci, pp. 1–51. https://doi.org/10.1016/B978-0-08-095975-7.00301-6.

Ruffell, A., Simms, M.J., Wignall, P.B., 2016. The Carnian Humid Episode of the late Triassic: a review. Geol. Mag. 153, 271–284. https://doi.org/10.1017/S0016756815000424.

Sadiq, M., 1988. Thermodynamic solubility relationships of inorganic vanadium in the marine environment. Mar. Chem. 23, 87–96. https://doi.org/10.1016/0304-4203(88)90024-2.

Safonova, I.Y., 2009. Intraplate magmatism and oceanic plate stratigraphy of the Paleo-Asian and Paleo-Pacific Oceans from 600 to 140 Ma. Ore Geol. Rev. 35, 137–154. https://doi.org/10.1016/j.oregeorev.2008.09.002.

Safonova, I.Y., Kojima, S., Nakae, S., Romer, R., Seltmann, R., Sano, H., Onoue, T., 2015. Oceanic island basalts in accretionary complexes of SW Japan: tectonic and petrogenetic implications. J. Asian Earth Sci. 113, 508–523. https://doi.org/10.1016/j.jseaes.2014.09.015.

Sato, H., Onoue, T., Nozaki, T., Suzuki, K., 2013. Osmium isotope evidence for a large Late Triassic impact event. Nat. Commun. 4, 2455. https://doi.org/10.1038/ncomms3455.

Schmidt, J.M., Rogers, R.K., 2007. Metallogeny of the Nikolai large igneous province (LIP) in southern Alaska and its influence on the mineral potential of the Talkeetna Mountains. In: Ridgway, K.D. (Ed.), Tectonic Growth of a Collisional Continental Margin: Crustal Evolution of Southern Alaska. Geol. Soc. Am. S, vol. 431, pp. 623–648. https://doi.org/10.1130/2007.2431(24).

Schmieder, M., Kring, D.A., 2020. Earth's impact events through geologic time: a list of recommended ages for terrestrial impact structures and deposits. Astrobiology 20, 91–141. https://doi.org/10.1089/ast.2019.2085.

Simms, M.J., Ruffell, A.H., 1989. Synchroneity of climatic change and extinctions in the late Triassic. Geology 17, 265–268. https://doi.org/10.1130/0091-7613(1989)017<0265:SOCCAE>2.3.CO;2.

Simms, M.J., Ruffell, A.H., 1990. Climatic and biotic change in the late Triassic. J. Geol. Soc. 147, 321–327. https://doi.org/10.1144/gsjgs.147.2.0321.

Simms, M.J., Ruffell, A.H., 2018. The Carnian Pluvial Episode: from discovery, through obscurity, to acceptance. J. Geol. Soc. 175, 989–992. https://doi.org/10.1144/jgs2018-020.

Simms, M.J., Ruffel, A.H., Johnson, A.L.A., 1995. Biotic and climatic changes in the Carnian (Triassic) of Europe and adjacent areas. In: Fraser, N.C., Sues, H.D. (Eds.), In the Shadow of the Dinosaurs: Early Mesozoic Tetrapods. Cambridge Univ. Press, pp. 352–365.

Smoliar, M.I., Walker, R.J., Morgan, J.W., 1996. Re–Os isotope constraints on the age of Group IIA, IIIA, IVA, and IVB iron meteorites. Science 271, 1099–1102. https://doi.org/10.1126/science.271.5252.1099.

Soua, M., 2014. Early Carnian anoxic event as recorded in the southern Tethyan margin, Tunisia: an overview. Int. Geol. Rev. 56, 1884–1905. https://doi.org/10.1080/00206814.2014.967315.

Stanley, G.D., 2003. The evolution of modern corals and their early history. Earth-Sci. Rev. 60, 195–225. https://doi.org/10.1016/S0012-8252(02)00104-6.

Stanley, G.D., Onoue, T., 2015. Upper Triassic reef corals from the Sambosan Accretionary complex, Kyushu, Japan. Facies 61, 1–27. https://doi.org/10.1007/s10347-014-0425-1.

Sugiyama, K., 1997. Triassic and lower Jurassic radiolarian biostratigraphy in the siliceous claystone and bedded chert units of the southeastern Mino Terrane. Central Japan. Bull. Mizunami Fossil Mus. 24, 79–193.

Sun, Y.D., Wignall, P.B., Joachimski, M.M., Bond, D.P.G., Grasby, S.E., Lai, X.L., Wang, L. N., Zhang, Z.T., Sun, S., 2016. Climate warming, euxinia and carbon isotope perturbations during the Carnian (Triassic) Crisis in South China. Earth Planet. Sci. Lett. 444, 88–100. https://doi.org/10.1016/j.epsl.2016.03.037.

Sun, Y.D., Richoz, S., Krystyn, L., Zhang, Z.T., Joachimski, M.M., 2018. Perturbations in the carbon cycle during the Carian Humid Episode: carbonate carbon isotope records from southwestern China and northern Oman. J. Geol. Soc. Lond. 176, 167–177. https://doi.org/10.1144/jgs2017-170.

Takahashi, S., Yamasaki, S., Ogawa, Y., 2014. Bioessential element-depleted ocean following the euxinic maximum of the end-Permian mass extinction. Earth Planet. Sci. Lett. 393, 94–104. https://doi.org/10.1016/j.epsl.2014.02.041.

Takaya, Y., Yasukawa, K., Kawasaki, T., Fujinaga, K., Ohta, J., Nakamura, K., Kimura, J.-I., Chang, Q., Hamada, M., Dodbiba, G., Nozaki, T., Liijima, K., Morisawa, T., Kuwahara, T., Ishida, Y., Kitazume, K., Fujita, T., Kato, Y., 2018. The tremendous potential of deep-sea mud as a source of rare-earth elements. Sci. Rep. 8, 5763. https://doi.org/10.1038/s41598-018-23948-5.

Takiguchi, T., Sugitani, K., Yamamoto, K., Suzuki, K., 2006. Biogeochemical signatures preserved in ancient siliceous sediments; new perspectives to Triassic radiolarian bedded chert compositions. Geochem. J. 40, 33–45. https://doi.org/10.2343/geochemj.40.33.

Tanner, L.H., Lucas, S.G., Chapman, M.G., 2004. Assessing the record and causes of late Triassic extinctions. Earth-Sci. Rev. 65, 103–139. https://doi.org/10.1016/S0012-8252(03)00082-5.

Tejada, M.L.G., Suzuki, K., Kuroda, J., Coccioni, R., Mahoney, J.J., Ohkouchi, N., Sakamoto, T., Tatsumi, Y., 2009. Ontong Java Plateau eruption as a trigger for the early Aptian oceanic anoxic event. Geology 37, 855–858. https://doi.org/10.1130/G25763A.1.

Tekin, U.K., 1999. Biostratigraphy and systematics of late Middle to late Triassic radiolarians from the Taurus Mountains and Ankara region. Turkey. Geol. Paläont. Mitt. Innsbr. Sonderbd. 5, 1–296.

Tokumaru, A., Nozaki, T., Suzuki, K., Goto, K.T., Chang, Q., Kimura, J.-I., Takaya, Y., Kato, Y., Usui, A., Urabe, T., 2015. Re-Os isotope geochemistry in the surface layers of ferromanganese crusts from the Takuyo Daigo Seamount, northwestern Pacific Ocean. Geochem. J. 49, 233–241. https://doi.org/10.2343/geochemj.2.0352.

Tozer, E.T., 1994. Canadian Triassic ammonoid faunas. Geol. Surv. Can. Bull. 467, 1–663.

Tribovillard, N., Algeo, T.J., Lyons, T.W., Riboulleau, A., 2006. Trace metals as paleoredox and paleoproductivity proxies: an update. Chem. Geol. 232, 12–32. https://doi.org/10.1016/j.chemgeo.2006.02.012.

Trotter, J.A., Williams, I.S., Nicora, A., Mazza, M., Rigo, M., 2015. Long-term cycles of Triassic climate change: a new $\delta^{18}O$ record from conodont apatite. Earth Planet. Sci. Lett. 415, 165–174. https://doi.org/10.1016/j.epsl.2015.01.038.

Turgeon, S.C., Creaser, R.A., 2008. Cretaceous oceanic anoxic event 2 triggered by a massive magmatic episode. Nature 454, 323–326. https://doi.org/10.1038/nature07076.

Uno, K., Onoue, T., Hamada, K., Hamami, S., 2015. Palaeomagnetism of Middle Triassic red bedded cherts from Southwest Japan: equatorial palaeolatitude of primary magnetization and widespread secondary magnetization. Geophys. J. Int. 189, 1383–1398. https://doi.org/10.1111/j.1365-246X.2012.05462.x.

Wakita, K., 1988. Origin of chaotically mixed rock bodies in the early Jurassic to early cretaceous sedimentary complex of the Mino terrane, Central Japan. Bull. Geol. Surv. Japan 39, 675–757.

Wanty, R.B., Goldhaber, M.B., 1992. Thermodynamics and kinetics of reactions involving vanadium in natural systems: accumulation of vanadium in sedimentary rocks. Geochim. Cosmochim. Acta 56, 1471–1483. https://doi.org/10.1016/0016-7037(92)90217-7.

Xu, G., Hannah, J.L., Stein, H.J., Bingen, B., Yang, G., Zimmerman, A., Weitschat, W., Mørk, A., Weiss, H.M., 2009. Re–Os geochronology of black shales in Arctic regions: evaluating the Anisian–Ladinian boundary and global faunal correlations. Earth Planet. Sci. Lett. 288, 581–587. https://doi.org/10.1016/j.epsl.2009.10.022.

Xu, G., Hannah, J.L., Stein, H.J., Mørk, A., Vigran, J.O., Bingen, B., Schutt, D.L., Lundschien, B.A., 2014. Cause of Upper Triassic climate crisis revealed by Re–Os geochemistry of Boreal black shales. Palaeogeogr. Palaeoclimatol. Palaeoecol. 395, 222–232. https://doi.org/10.1016/j.palaeo.2013.12.027.

Yamashita, D., Kato, H., Onoue, T., Suzuki, N., 2018. Integrated Upper Triassic conodont and radiolarian biostratigraphies of the Panthalassa Ocean. Paleontol. Res. 22, 167–197. https://doi.org/10.2517/2017PR020.

Yao, A., Matsuda, T., Isozaki, Y., 1980. Triassic and Jurassic radiolarians from the Inuyama area, Central Japan. J. Geosci. Osaka City Univ. 23, 135–154.

Zamoras, L.R., Matsuoka, A., 2004. Accretion and postaccretion tectonics of the Calamian Islands, North Palawan block. Philippines. Isl. Arc 13, 506–519. https://doi.org/10.1111/j.1440-1738.2004.00443.x.